OPTICAL INVESTIGATION OF BISMUTH SELENIDE (Bi_2Se_3) AND ANTIMONY TELLURIDE (Sb_2Te_3)

by

MULAYE DORCAS

21000102

A dissertation submitted to the Department of Physics
of The University of Zambia
in partial fulfillment of the requirements for the award of the degree of
Master of Science in Physics

March 2024

Copyright

Declaration

I, Dorcas Mulaye, declare that this is my own work and that to the best of my knowledge has never been produced or presented by any other person.

Approval

This dissertation of Dorcas Mulaye is approved as a partial fulfilment of the requirements for the award of the Degree of Master of Science in Physics, of the University of Zambia.

Examiners' Signatures

Examiner 1
Name: ....Date: ....

Signature: ....

Examiner 2
Name: ....Date: ....

Signature: ....

Examiner 3
Name: .... Date: ....

Signature: ....

Supervisor: .... Date: ....

Signature: ....

Dedication

To my beloved husband,

This dissertation is dedicated to you, my source of endless support, love, and encouragement. Your unwavering belief in me has been my greatest strength throughout this journey. Thank you for your patience, understanding, and sacrifices. Without you by my side, none of this would have been possible. This achievement is as much yours as it is mine.

With all my love and gratitude.

Acknowledgments

I would like to express my deepest gratitude to the following individuals and organizations who have supported and guided me throughout the completion of this dissertation:

I would like to thank Dr.Geoffrey Chanda, my principle supervisor for allowing me to do research under his guidance and support; wonderful discussions and providing good conducive working environment during my period of research at the Department of Physics of the University of Zambia and at the Universitat Stuttgart.
I also extend my thanks to Dr Sylvester Hatwaambo, for accepting to be my co−supervisor and ISP (International Science Program) for paying my tuition fees.

I am also thankful to Mr Godfrey Banda and Professor Recab O. Manyala of the University of Zambia, Dr Margaret Samiji of the University of Dar-Es-Salaam, and Dr. Mario Piva of the Max Planck Institute of the Chemicals and solids for their invaluable assistance and advice during my course of research at the University of Zambia, University of Dar-Es-Salaam and Max Planck Institute respectively.

Lastly, I would like to express my appreciation to my family and friends for their unwavering support and encouragement throughout this journey.

ABSTRACT

This dissertation is devoted to the investigation of the optical properties of two topological insulators, Bismuth Selenide (Bi_2Se_3) and Antimony Telluride (Sb_2Te_3), by optical spectroscopy reflection measurements in a wide frequency range (500 – 40000 cm^{-1}) and temperature (13 to 300 K) . Utilizing Kramers-Kronig analysis, complex conductivity is calculated from which other optical properties are obtained. The resistivity of both samples demonstrates metallic behavior with residual resistivity ratios of 1.8 for Bi_2Se_3 and 7.5 for Sb_2Te_3, indicating purer samples. From the study it is found that near-infrared optical conductivity for Bi_2Se_3 is dominated by bulk carriers and shows a linear-in-frequency increase in the frequency range from 1500 to 3000 cm^{-1}, reflecting transitions between bands with complex dispersion. This linearity might be interpreted as a signature of three-dimensional (bulk) Dirac bands. However, no linearity is observed in Sb_2Te_3. The Drude like contribution at low frequencies may be a signature of surface states contribution to the conductivity. Spectral weight analysis offers insights into the distribution of optical weight with temperature and frequency, revealing the influence of correlation effects and charge excitations on low-energy electrodynamics. Reflectivity measurements on the Bi_2Se_3 sample crystal reveal insights into its metallic behavior, with a plasma-like feature attributed to Dirac surface states. Direct band gaps and interband transitions characterize its optical properties, with certain transitions exhibiting temperature dependence. Conductivity analysis provides information about charge carrier behavior and scattering mechanisms, revealing the influence of electron-phonon coupling and electronic band structure on charge transport. Similarly, temperature-dependent trends in reflectivity for Sb_2Te_3 unveil complex spectral weight transfers and interband transitions, challenging conventional Drude theory predictions. Conductivity analysis shows conductivity decreasing at low frequencies due to phonon scattering and increasing at higher frequencies accompanied by the emergence of a Near Infra-Red (NIR) band.

Contents

List of Figures

List of Tables

List of Abbreviations and Symbols

Bi_2Se_3	Bismuth Selenide
Sb_2Te_3	Antimony Telluride
NIR	Near Infra-Red
DC	Direct Current
THz	Terahertz
IR	Infra-Red
IQHE	Integer Quantum Hall Effect
FTIR	Fourier-Transform Infrared
HgTe	Mercury Telluride
UV/VIS/NIR	Ultraviolet/Visible/Near Infra-Red
BiSb	Bismuth Antimony
Bi_2Te_3	Bismuth Telluride
σ	Conductivity
ρ	Resistivity
τ	Relaxation time
ω	Frequency
m^*	Effective mass
ϵ	Dielectric constant
Γ	Scattering rate

Chapter 1

1 INTRODUCTION

In condensed matter Physics, different phases of matter are usually classified by considering what symmetries they break. This paradigm is due to Landau who stated that a particular symmetry property exists or does not exist; for example in liquid crystals where translational symmetry is broken, magnets where rotational symmetry is broken, and it is more abstract in superconductors, where gauge symmetry is broken [1]. The emergence of a topological description reflects a type of order in condensed matter Physics that is quite different from conventional orders described in terms of system breaking. One feature that distinguishes topological phases is that they are typically measurable physical properties with extremely precise quantization as a result of insensitivity of topology to perturbations such as defects and thermal fluctuations. The first example was the transverse hall conductance in the integer quantum hall effect (IQHE) [2]. In the quantum Hall effect, a strong magnetic field confines the motion of electrons in the bulk, but the same field forces them into delocalized edge states on the surface. A two-dimensional metal in strong magnetic field is thus an insulator in the bulk, but conduct along the surface, via a discrete number of completely open edge state channels. The number of edge state channels was linked to the Chern number, a topological invariant of the occupied bands [3]. However, topological order until recently was only observed in two-dimensional electron gases under extreme conditions of low temperature and high magnetic field. The present fascination in this field results from the experimental discovery that there are topological phases in fairly ordinary materials that occur in three dimensions and zero magnetic field [4, 5]. The name topological insulator was coined for such systems, and their study became a blossoming branch of solid state Physics. Following the theoretical prediction [6], electronic transport measurements confirmed that a thin layer of Mercury Telluride (HgTe) is a topological insulator [7]. Since that time, a host of materials, including the Bismuth compounds like Bismuth Antimony (BiSb), Bismuth Selenide (Bi_2Se_3) and Bismuth Telluride (Bi_2Te_3) were discovered to be three-dimensional topological insulators [8, 9, 10, 11].

Sub terahertz (THz) and infrared (IR) spectroscopy allows for one to explore a multitude of electronic processes vital to understanding the Physics of topological insulators. The processes include the electromagnetic response of both bulk and surface state charge carriers, the electronic structure at the edge of the bulk energy gap, as well as optical excitations of higher energy due to the complex band minima/maxima of the bulk gap. Moreover, the instrumentation used to achieve this enables experiments covering these energy ranges to be performed in high magnetic fields. The aim of this dissertation was to Investigate the optical properties of two topological insulators Bi_2Se_3 and Sb_2Te_3 in the mid and near infrared region. To achieve this aim, two samples (i.e., Bi_2Se_3 and Sb_2Te_3 single crystals in the millimetre ranges) were investigated by use of reflectivity measurements. From these measurements, optical conductivities have been obtained through Krammers-Kronig analysis. From the optical conductivity, the gap symmetries as well as many other relevant phenomena connected with topological insulators have been obtained (the details are given in the course of this dissertation). The current dissertation is organized as follows: I first review the optical properties of solids, general properties of topological insulators, and some of the most important concepts and physical properties of topological insulators in Chapter 2. This is followed by brief experimental descriptions of optical-spectroscopy techniques and the analysis of optical data in Chapter 3 and 4, respectively. Finally, the results and discussions for the samples (i.e., Bi_2Se_3 and Sb_2Te_3) considered in this research and the conclusions are presented in Chapters 5 and 6 respectively.

1.1 Aim/Purpose of the study

To investigate the optical properties of two topological insulators (Bi_2Se_3 and Sb_2Te_3 single crystals), using infrared spectroscopy.

1.2 Specific Objectives

(i) To calibrate the UV/VIS/NIR Perking Elmer Lambda 1050+ spectrometer at the University of Dar es Salaam by using data obtained using the Bruker vertex 80 at the University of Stuttgart as reference standard fit.
(ii) To measure the reflectivity of Bi_2Se_3 and Sb_2Te_3 in the infrared region
(iii) To determine the conductivity of Bi_2Se_3 and Sb_2Te_3 using Kramers–Kronig analysis method.

1.3 Research Questions

(i) How does the optical response of Bi_2Se_3 and Sb_2Te_3 crystals obtained in the study compare with those of other topological insulators already known?
(ii) How does the Direct Current (DC) conductivity of Bi_2Se_3 and Sb_2Te_3 compare with the optical conductivity at low frequencies?

1.4 Significance of the study

The knowledge obtained from the characterization of optical properties of Bi_2Se_3 and Sb_2Te_3 topological insulators in this study will add to the wealth of knowledge in the field of Condensed Matter Physiscs.

Chapter 2

2 THEORETICAL BACKGROUND AND LITERATURE REVIEW

2.1 Optical properties of Solids

A solid is a state of matter that retains its shape and volume when not confined. A metal is of such a class and is held together by metallic bonds, conducts heat and electricity, reflects light, and whose resistivity usually decreases with decreasing temperature with electron bands that are partially filled. In a metal, the electrodynamics are a result of the intraband and interband transitions respectively. Intraband transitions are optical transitions between electronic states in the bands while interband transitions are transitions between different bands [12]. At room temperature, electrical conduction of metals shows two characteristics of which the first is that there is a linear relation between the electric current I, that flows through the sample and the voltage V, that drops between the two ends of the sample:

$$\frac{I}{V} = G = \frac{1}{R} \tag{1}$$

where $G(\frac{1}{R})$ is the conductance of the sample. The second characteristic is that the conductivity of a material, σ_i , is given by:

$$\sigma_i = \frac{G_i L_i}{A_i} = \frac{1}{\rho_i} \tag{2}$$

where L$_i$ is the length of the sample, A$_i$ is the area of its cross section and ρ is the resistivity of the sample. The material-specific quantity is called the conductivity. Conductors obeying these relations are referred to as ohmic conductors. Frequency dependant optical properties of metals can be described by microscopic theories (e.g Drude-Lorentz model) that rely on models involving impurities, lattice vibrations, and electron scattering within the material. Electrical conduction in pure nanostructures at low temperature might deviate from the ohmic case as in the case of this study of topological insulators.

2.2 Microscopic theories

Optical properties of solids are best described by microscopic theories such as Drude-Sommerfeld model for metals, and Lorentz model for semiconductors and insulators.

2.2.1 The Drude-Sommerfeld model

The Drude-Sommerfield model, regards a metal as a classical gas of electrons which are able to move freely in the lattice without any interaction between them or rather have diffusive motion. With the scattering rate, $(\frac{1}{\tau})$, and the mass of electrons being independent of the velocity (energy). The central assumption of the model is that there exists an average relaxation time, τ, which takes the system into equilibrium and the equation of motion for an electron in the presence of an applied electric field is given by:

$$m\frac{d^2r}{dt^2} + m\frac{\nu}{\tau} = -eE \tag{3}$$

with $\frac{dr}{dt}$ being the velocity and the current density

$$j = ne\nu \tag{4}$$

where n is the density of charge carriers, m is the charge carrier mass, and e is the electronic charge respectively.
By applying an alternating electric field of the form:

$$E(t) = E_0 e^{-i\omega\tau} \tag{5}$$

the Drude-Sommerfield model gives rise to relationships among the material properties and optical constants as summarized by Chanda [13] in table 1.

Table 1: Relationships among material properties and optical constants [13].

	Dielectric constant $\widehat{\epsilon}$	Conductivity $\widehat{\sigma}$	Refractive index $\widehat{N}$
$\widehat{\epsilon}$	$\widehat{\epsilon} = \epsilon_1 + i\epsilon_2$	$\epsilon_1 = 1 - \frac{4\pi\sigma_2}{\omega}$ $\epsilon_2 = \frac{4\pi\sigma_1}{\omega}$	$\epsilon_1 = \frac{n^2-k^2}{\mu_1}$ $\epsilon_2 = \frac{2nk}{\mu_1}$
$\widehat{\sigma}$	$\sigma_1 = \frac{\omega\epsilon_2}{4\pi}$ $\sigma_2 = (1-\epsilon_1)\frac{\omega}{4\pi}$	$\widehat{\sigma} = \sigma_1 + i\sigma_2$	$\sigma_1 = \frac{nk\omega}{2\pi\mu_1}$ $\sigma_2 = (1 - \frac{n^2-k^2}{\mu_1})\frac{\omega}{4\pi}$
$\widehat{N}$	$n = \{\frac{\mu_1}{2}[\epsilon_1^2 + \epsilon_2^2]^{1/2} + \frac{\epsilon_1\mu_1}{2}\}^{1/2}$ $k = \{\frac{\mu_1}{2}[\epsilon_1^2 + \epsilon_2^2]^{1/2} - \frac{\epsilon_1\mu_1}{2}\}^{1/2}$	$n = \{\frac{\mu_1}{2}[(1 - \frac{4\pi\sigma_2}{\omega})^2 + (\frac{4\pi\sigma_1}{\omega})^2]^{1/2} + \frac{\mu_1}{2} - \frac{2\pi\mu_1\sigma_2}{\omega}\}^{1/2}$ $k = \{\frac{\mu_1}{2}[(1 - \frac{4\pi\sigma_2}{\omega})^2 + (\frac{4\pi\sigma_1}{\omega})^2]^{1/2} - \frac{\mu_1}{2} + \frac{2\pi\mu_1\sigma_2}{\omega}\}^{1/2}$	$\widehat{N} = n + ik$

In general, only the reflectivity and transmittance are accessible by optical experiments which can be evaluated through the optical constants n and k, i.e.,

$$R = \frac{(1-n)^2 + k^2}{(1+n)^2 + k^2} \tag{6}$$

and,

$$T_r = 1 - (A + R) \tag{7}$$

where R is the reflectivity, T_r is the transmission coefficient (transmittance), A is the absorption, n is the real part of the refractive index, and k is the imaginary part of the refractive index.

From the reflectivity and transmission coefficients, the complex conductivity can be obtained either through the Fresnel formulas or Kramers-Kronig analysis. The Kramers-Kronig analysis is not always possible (e.g. due to a limited frequency range available for the measurement, or samples which are not opaque). In this dissertation, Krammers-Kronig Analysis was used as a method, since the samples were opaque and the frequency range was wide enough.

Although the Drude-Sommerfield model has been used for a long time and it is frequently used today, there is need for modification, so that the frequency dependence of the scattering rate and electron band mass is taken into consideration. Several conducting materials, which are of current interest in the ongoing condensed matter research, are influenced by electron-electron interaction. This is particularly true in systems with d and f electrons, where the scattering of extended states with localized or narrow-band states may occur and in materials deviating from the conventional Fermi-liquid scenario. In such cases, it turns out that a simple Drude-Sommerfield behavior assuming a constant scattering rate and band mass m is no longer appropriate. This calls for the necessity to extend the original Drude-Sommerfield model to a more generalized formulation, the so-called extended Drude-Sommerfield model, which takes into account the frequency dependence of the scattering rate,$\frac{1}{\tau}(\omega)$ and effective mass, $m^*(\omega)$.

2.2.2 Lorentz model

Unlike in the Drude-Sommerfield model, the Lorentz model best describes optical properties of band semiconductors and insulators. These materials have a band gap that separates the completely filled valence band and the empty conduction band at zero temperature, and their Fermi surface lies between two bands meaning that there is lack of dc conduction and finite static dielectric constants. Inter-band transitions in these materials are responsible for their electrodynamic properties. In the Lorentz model, the equation of motion for an electron in the presence of a field is given by:

$$m\frac{d^2r}{dt^2} + m\frac{v}{r} + m\omega_0^2 r = -eE(t) \tag{8}$$

where the terms are as defined in the Drude-Sommerfield model with an additional term called the restoring force denoted as $m\omega_0^2 r$,

$$\omega_0 = \sqrt{\frac{k}{m}} \tag{9}$$

is the centre frequency or oscillator frequency, as this model is that of a harmonic oscillator. With

$$E = E_0 \exp(-i\omega t), \tag{10}$$

r is found to be equal to:

$$r = \frac{\frac{-eE}{m}}{(\omega_0^2 - \omega^2) - \frac{i\omega}{\tau}}. \tag{11}$$

Solving the equation of motion gives the complex conductivity:

$$\hat{\sigma}(\omega) = \frac{ne^2}{m} \frac{\omega}{i(\omega_0^2 - \omega^2) + \frac{\omega}{\tau}} \tag{12}$$

where $\frac{1}{\tau}$ in this case describes the broadening of the oscillator, and $\omega_p = (\frac{4\pi ne^2}{m})^{\frac{1}{2}}$ describes the oscillator strength and is called the plasma frequency. Thus, solving for the real and imaginary parts of the complex conductivity gives the equations below as confirmed by Chanda [13] ,

$$\sigma_1(\omega) = \frac{\omega_p^2}{4\pi} \frac{\frac{\omega^2}{\tau}}{(\omega_0^2 - \omega^2)^2 + \frac{\omega^2}{\tau^2}} \tag{13}$$

and,

$$\sigma_2(\omega) = \frac{\omega_p^2}{4\pi} \frac{\omega(\omega_0^2 - \omega^2)}{(\omega_0^2 - \omega^2)^2 + \frac{\omega^2}{\tau^2}} \tag{14}$$

In this model, the reflectivity starts from a value different from 1. When the value of optical reflectivity is 1, it means that all the incident light is reflected at the surface of the material, and none is transmitted into or absorbed by the material.

$$R = \left| \frac{n-1}{n+1} \right|^2 \tag{15}$$

and increases at ω_0 which is related to the difference in energies between two energy states or the energy of a semiconductor. The reflectivity drops at the plasma frequency of the localized excitations (ω_p). It is important to note the three frequencies of particular relevance in this model which are: $\frac{1}{\tau}$, ω_0, and ω_p, giving rise to four different regimes which are: low frequency regime for $\omega < \left(\omega_0 - \frac{1}{\tau}\right)$, the absorption regime for $\omega_0 - \frac{1}{2\tau} < \omega < \omega_0 + \frac{1}{2\tau}$, the reflection regime for $\omega_0 + \frac{1}{\tau} < \omega < \omega_p$, and the transparent regime for $\omega > \omega_p$.

2.2.3 Extended Drude analysis

In systems with d and f electrons where the scattering of extended states with narrow band states could take place and in materials deviating from the conventional Fermi-liquid scenario, (several conducting materials are shaped in their electronic properties by the electron to electron interaction), the assumption of a constant scattering rate and a band mass m_o is no longer applicable as in the case of a simple Drude behavior. Thus, there's need for an extended Drude (the so called generalised Drude model) which satisfies:

$$\hat{\sigma}(\omega) = \sigma_{1D}(\omega) + i\sigma_{2D}(\omega) = \frac{\omega_p^2}{4\pi} \frac{1}{\Gamma(\omega) - i\omega \frac{m^*(\omega)}{m_b}} \tag{16}$$

where,
m^* is the effective mass and Γ is the scattering rate.
By inverting equation 16, we obtain:

$$\Gamma(\omega) = \frac{1}{\tau(\omega)} = \frac{1}{\frac{\omega_p^2}{4\pi} \frac{\sigma_{1D}(\omega)}{|\sigma_D|^2}} \tag{17}$$

and

$$\frac{m^*(\omega)}{m_b} = \frac{\omega_p^2}{4\pi}\frac{\sigma_{2D}(\omega)}{\omega\,|\sigma_D|^2} \tag{18}$$

Which are the Scattering rate and the mass enhancement factor and can be expressed graphically from analysis of optical conductivity.

2.3 Optical Spectroscopy

Optical spectroscopy is a powerful method useful in the characterization of new materials and for investigating the properties of many solids of current interest, e.g. topological insulators, superconductors, heavy-fermions systems, low-dimensional conductors with charge- and spin-density wave instabilities. Its potential rests on a number of characteristics, among which is the broad range of operating frequencies, contactless measurements, the possibility of probing the electronic subsystem directly, and extracting relevant information of such fundamental significance as the characteristic excitation energies, concentration of carriers, the mobility and relaxation frequency of carriers, superconducting gaps, vibrational degrees of freedom, charge-transfer gaps, and pseudo gaps. In order to investigate a given material successfully by optical means, the availability of a wide frequency range is necessary. Optical spectroscopy is based on investigating the behavior of optical parameters (conductivity, spectral weight, scattering rate, and mass enhancement), as a function of frequency and temperature and among the methods of optical spectroscopy are terahertz and infrared Fourier-transform spectroscopy of these two experimental techniques, infrared Fourier-transform spectroscopy has been used extensively in this dissertation work and is hereby briefly reviewed.

2.4 Infrared Spectroscopy

According to section 3.2 of [13], Fourier-transform infrared (FTIR) spectroscopy is the most used method of infrared spectroscopy. In this method, infrared radiation is focused on the sample where it is either transmitted or reflected. Apart from reflection and transmission, some of the incident infrared radiation is absorbed by the sample. The resulting spectrum is like a fingerprint; no two materials produce the same infrared spectrum, making infrared spectroscopy a useful tool for several types of analysis. With FTIR spectroscopy, all of the infrared frequencies arriving at the detector are measured simultaneously, rather than individually. This is achieved by employing an interferometer producing a unique signal. The signal can be measured very quickly, usually on the order of a second or so. Most interferometers employ a beam splitter, which divides the incoming infrared beam into two optical beams. One beam reflects off a flat mirror which is fixed, while the other beam reflects off a flat mirror, which can be moved over a short distance (typically a few millimeters). The two beams are recombined when they meet back at the beam splitter. Due to the different optical lengths these two beams interfere with each other and the resulting interferogram has the unique property that every data point (a function of the moving mirror position x), has information about every infrared frequency, which comes from the source. This means that as the interferogram is measured; all frequencies are being measured simultaneously. By employing a Fourier transformation, the desired spectral information for further analysis is obtained and thus the use of the interferometer results in extremely fast measurements. Because the analyst requires a frequency spectrum (a plot of the intensity at each individual frequency) in order to make identification, the measured interferogram signal cannot be interpreted directly. A means of “decoding” the individual frequencies is required. This is accomplished via a well known mathematical technique called the Fourier transformation. This transformation is performed by the computer which then presents the user with the desired spectral information for analysis. A background spectrum is also to be measured due to the need for the absorption intensity which is usually a measurement without a sample on the beam which can then be compared to the measurement with the sample on the beam to determine the "percentage reflectance or transmittance". At the end of it all, all spectral features which are present are strictly due to the sample since all the instrumental characteristics are removed by the technique.

2.4.1 Advantages of FTIR spectroscopy

Some of the major advantages of FTIR spectroscopy include:

1. Fast measurement since all frequencies are measured simultaneously

2. Mechanical simplicity considering the fact that the moving mirror is the only continuously moving part in the interferometer. This also reduces chances of mechanical breakdown

3. The instruments are internally self calibrated

4. Improved sensitivity due to the presence of highly sensitive detectors

The advantages named here, together with several others, make make measurement made by FTIR extremely accurate and reproducible.

2.4.2 Normal operation of the FTIR spectrometer

The normal operation for the instrument as recorded in [14] is as follows:

1. The source: Infrared energy is emitted from glowing black body source. These sources could be mercury lamp for FIR (far infrared), globar for MIR (mid infrared), or tungsten lamp for NIR (near infrared). The beam from these sources passes through an aperture which controls the amount of en-

ergy to the sample(and ultimately to the detector).

2. The interferometer: the beam passes the interferometer where the "spectral encoding" takes place. The resulting interferogram signal then exits the interferometer.

3. The sample: the beam enters the sample compartment where it is transmitted through or reflected depending on the type of analysis being accomplished (it was reflected on our sample because it was totally opaque solid single crystals).

4. The Detector: the beam finally passes to the detector for final measurement. The detectors used are specially designed to measure the special interferogram signal e.g. Bolometer for the far infrared (FIR) signal, MCT (Mercury Carbide Telluride)for the mid infrared (MIR) signal and in Sb (antimonide) detector for the near infrared (NIR) signal.

5. The computer: the measured signal is digitized and sent to the computer where the Fourier transformation takes place. The final infrared spectrum is then presented to the user for interpretation and any further manipulation.

2.5 Topological Insulators

In order for the above spectroscopy techniques to be effectively carried out, the background knowledge of the samples being used(Bi_2Se_3 and Sb_2Te_3 which are classified as topological insulators) is essential for precise measurements to be carried out. Topological insulators are a class of materials that exhibit unique electronic properties due to their topology. On the other hand, topology is a branch of mathematics dealing with the properties of space that are preserved under continuous deformations, such as stretching, crumpling, and bending. Some examples of topological insulators include

Bi_2Se_3, Sb_2Te_3, HgTe, Bi_2Te_3, and $Bi_1 - xSbx$. In topological insulators, the electronic structure is characterized by non-trivial topology, leading to protected conducting states on their surfaces or edges.

The key concept in topological insulators is the notion of a band topology, which describes how electronic bands in a material are connected in momentum space. In a topological insulator, there is a band inversion between the valence and conduction bands, resulting in a band gap in the bulk and conducting states on the surface or edge. These surface or edge states are topologically protected, meaning they are robust against perturbations that do not break certain symmetries.

2.5.1 Band Theory of Topological Insulators

Band theory is a foundational concept in condensed matter Physics that explains the behavior of electrons in crystalline solids. It provides a framework for understanding how electrons occupy energy levels, known as bands, within a solid material. In the context of topological insulators, band theory plays a crucial role in elucidating the electronic properties that give rise to their unique characteristics. Here are some key points to understand about band theory in the context of topological insulators:

Energy Bands: In a crystalline solid, the arrangement of atoms leads to the formation of energy bands, which represent the allowed energy states for electrons. The electronic band structure is determined by the periodic potential of the crystal lattice.

Band Gap: The energy bands are separated by regions called band gaps, where no electron states are allowed. The size of the band gap influences the electrical and optical properties of the material.

Fermi Level: The Fermi level is the energy level at which the probability of finding an electron is equal to 0.5 at absolute zero temperature. It lies within the band gap for insulators and in the conduction or valence band for conductors.

Bloch's Theorem: Bloch's theorem states that the wave function of an electron in a periodic potential can be expressed as the product of a plane wave and a periodic function with the same periodicity as the lattice. This theorem allows for the description of electronic states in crystalline materials.

Brillouin Zone: The Brillouin zone is the unit cell in reciprocal space that represents all possible states of a periodic crystal lattice. It plays a crucial role in understanding the electronic band structure and symmetry properties of materials.

Band Structure Calculations: The electronic band structure of materials can be calculated using techniques such as density functional theory (DFT) or tight-binding models. These calculations provide insight into the energy levels and dispersion relations of electrons in the material.

Topology and Band Theory: In topological insulators, the band structure exhibits non-trivial topology, leading to protected surface or edge states. These topological properties arise due to band inversion and the presence of certain symmetries in the material's electronic structure.

2.5.2 Topological Concepts in Topological Insulators

Berry Phase (Berry Connection):
The Berry connection $\mathbf{A}(\mathbf{k})$ and the associated Berry curvature $\mathbf{F}(\mathbf{k})$ are fundamental quantities characterizing the topology of electronic bands.

The Berry connection is given by:

$$\mathbf{A}(\mathbf{k}) = -i\langle u_{\mathbf{k}}|\nabla_{\mathbf{k}}|u_{\mathbf{k}}\rangle \tag{19}$$

The Berry curvature is the curl of the Berry connection:

$$\mathbf{F}(\mathbf{k}) = \nabla_{\mathbf{k}} \times \mathbf{A}(\mathbf{k}) \tag{20}$$

These quantities describe the geometric phase acquired by an electron wavefunction as it adiabatically traverses a closed loop in momentum space.

2. **Chern Number (Topological Invariant)**:
The Chern number C is a topological invariant characterizing the topology of a band structure. For a two-dimensional Brillouin zone, the Chern number is given by:

$$C = \frac{1}{2\pi}\int_{BZ} \mathbf{F}(\mathbf{k}) \cdot d\mathbf{S} \tag{21}$$

The integral is taken over the entire Brillouin zone (BZ). The Chern number distinguishes between topologically distinct phases of matter and determines the presence of edge states.

3. **Z2 Invariant (Topological Classification)**:
The Z2 invariant is another topological invariant used to classify topological insulators. It is calculated based on the parity of certain symmetry-protected quantities such as the Pfaffian of the Berry connection matrix. The Z2 invariant takes values of 0 or 1 and distinguishes between different topological phases.

4. **Edge or Surface States (Dispersion Relation)**:
The dispersion relation $E(k)$ describes the energy-momentum relationship of surface or edge states in topological insulators. Depending on the specific symmetry properties and dimensionality of the system, the dispersion relation may take different forms, such as linear, quadratic, or Dirac-like. The

presence of dispersion-less surface states within the bulk band gap is a hallmark feature of topological insulators.

Understanding these topological concepts and associated formulas is crucial for characterizing the unique electronic properties of topological insulators and predicting their behavior in different material systems. These concepts provide a theoretical framework for understanding the topological nature of electronic band structures and their potential applications in emerging technologies.

2.5.3 Berry Phase and Berry Connection in Topological Insulators

Berry Phase (Berry Connection): The Berry phase is a geometric phase acquired by the wavefunction of a quantum system as it evolves along a closed path in parameter space. It characterizes the geometric and topological properties of the quantum states. The Berry connection, denoted by $\mathbf{A}(\mathbf{k})$, is a vector potential in momentum space that governs the evolution of the quantum state. The Berry connection is defined as:

$$\mathbf{A}(\mathbf{k}) = -i\langle u_{\mathbf{k}}|\nabla_{\mathbf{k}}|u_{\mathbf{k}}\rangle \tag{22}$$

where $|u_{\mathbf{k}}\rangle$ is the periodic part of the Bloch wavefunction and $\nabla_{\mathbf{k}}$ is the gradient with respect to momentum.

Berry Curvature:
The Berry curvature, denoted by $\mathbf{F}(\mathbf{k})$, is the curl of the Berry connection and is a measure of the geometric phase acquired by the wavefunction. It quantifies the curvature of the quantum state space and is related to the

topology of the electronic bands. The Berry curvature is given by:

$$\mathbf{F}(\mathbf{k}) = \nabla_{\mathbf{k}} \times \mathbf{A}(\mathbf{k}) \tag{23}$$

Understanding the Berry phase and Berry connection is essential for unraveling the topological nature of electronic band structures in topological insulators and other topological materials.

2.5.4 Bulk-Edge Correspondence in Topological Insulators

Bulk-edge correspondence is a fundamental principle in topological insulators that establishes a connection between the bulk and edge (or surface) properties of a material.

Topological Invariants: Topological invariants, such as Chern numbers or Z2 indices, characterize the bulk electronic structure of topological insulators. These invariants are integer-valued quantities that encode the global topology of the electronic bands.

Edge (or Surface) States: Topological insulators exhibit topologically protected edge or surface states within the bulk band gap. These states arise due to the non-trivial topology of the electronic structure and are robust against disorder or imperfections.

Robustness: Edge or surface states are robust against local perturbations that do not break certain symmetries, such as time-reversal symmetry or inversion symmetry. They cannot be removed without closing the bulk band gap, making them topologically protected.

Bulk-Edge Correspondence Principle: The presence of topologically protected edge or surface states is directly related to the bulk topological invariants of the material. For example, in a two-dimensional topological insulator, the number of edge states is determined by the Chern number of the bulk band structure.

Bulk-edge correspondence is a fundamental principle that lies at the heart of the unique electronic properties of topological insulators and is instrumental in their exploration and utilization in various technological applications.

2.5.5 Topological Invariants in Topological Insulators

Topological invariants are mathematical quantities used to characterize the topological properties of electronic band structures in materials, particularly in topological insulators.

Classification of Topological Phases: Topological invariants classify different topological phases of matter based on their electronic band structures. They distinguish between trivial and non-trivial electronic states, capturing the global topology of the bands.

Types of Topological Invariants: In topological insulators, common types of topological invariants include Chern numbers, Z2 indices, and winding numbers. These invariants capture different aspects of the electronic band structure and provide information about the presence of topologically protected states.

Chern Number: The Chern number is a topological invariant defined for two-dimensional systems with broken time-reversal symmetry. It quantifies the total Berry curvature integrated over the Brillouin zone and determines the presence of chiral edge states.

Z2 Invariant: The Z2 invariant is a topological invariant used for systems with time-reversal symmetry. It classifies materials into different topological phases based on the parity of certain band eigenvalues.

Winding Number: The winding number is another topological invariant applicable to one-dimensional systems, such as topological insulators with chiral edge states. It quantifies the winding of the phase of the wave-function around the Brillouin zone and characterizes the topology of the band structure.

Understanding topological invariants is essential for unraveling the topological nature of electronic band structures in topological insulators and other topological materials, enabling the discovery of new Physics and technological advancements.

2.5.6 Symmetry considerations

Symmetry considerations play a crucial role in determining the topological properties of materials, including topological insulators. Symmetries such as time-reversal symmetry, inversion symmetry, and particle-hole symmetry profoundly influence the electronic band structure and can lead to the emergence of topologically protected states. Here's how each symmetry affects the topological properties of materials:

Time-Reversal Symmetry (TRS):
Time-reversal symmetry states that the Hamiltonian of a physical system remains unchanged under the reversal of time. In topological insulators, time-reversal symmetry plays a pivotal role in protecting the spin-momentum locking of edge or surface states. Materials with time-reversal symmetry typically exhibit non-trivial band structures with spin-polarized edge states, as observed in the quantum spin Hall effect. Breaking time-reversal symmetry can lead to the emergence of the quantum anomalous Hall effect, characterized by the presence of chiral edge states and a quantized Hall conductance.

Inversion Symmetry:

Inversion symmetry refers to the spatial inversion of a crystal lattice, where the positions of atoms are reversed relative to a chosen point or axis. In topological insulators, inversion symmetry often works in conjunction with time-reversal symmetry to protect the topological properties of materials. Materials with inversion symmetry can exhibit non-trivial band gaps and topologically protected surface states, as seen in certain classes of three-dimensional topological insulators.

Particle-Hole Symmetry:

Particle-hole symmetry relates the electron states above the Fermi energy to the hole states below the Fermi energy in a material. In topological insulators, particle-hole symmetry can protect the topological properties of the material and ensure the presence of gapless edge or surface states. Breaking particle-hole symmetry may lead to the emergence of superconductivity or other exotic electronic phases, which can modify the topological properties of the material.

2.6 Edge and Surface States in Topological Insulators

Edge and surface states are unique electronic states that emerge at the boundaries of topological insulators due to their non-trivial bulk topology. These states are topologically protected, robust against disorder, and exhibit interesting properties such as spin-momentum locking.

Derivation of Dispersion Relations and Wave Functions:

1. Effective Mass Approximation:

In the effective mass approximation, the dispersion relation near the band extrema is approximated as parabolic, allowing for the treatment of electrons as particles with effective masses.The effective mass approximation simplifies the analysis of edge and surface states by considering the dynamics of electrons near the Fermi level.

2. Tight-Binding Models:
Tight-binding models provide a microscopic description of the electronic structure of materials by considering the hopping of electrons between neighboring lattice sites. By solving the tight-binding Hamiltonian, one can obtain the dispersion relation and wave functions of edge or surface states in topological insulators.

Procedure for solving the tight-binding Hamiltonian:

1. Effective Mass Approximation:
Near the band extrema, the dispersion relation can be approximated as:

$$E(k) = E_0 + \frac{\hbar^2 k^2}{2m^*} \tag{24}$$

where E_0 is the energy at the band extrema, k is the wave vector, and m^* is the effective mass. By solving the Schrödinger equation for the effective mass Hamiltonian, one can obtain the wave functions of edge or surface states.

2. Tight-Binding Models:
The tight-binding Hamiltonian includes terms for nearest-neighbor and next-nearest-neighbor hopping of electrons. By diagonalizing the tight-binding Hamiltonian matrix, one can find the eigenvalues and eigenvectors, which correspond to the energy levels and wave functions of the system. The dispersion relation can be obtained by plotting the energy as a function of the wave vector along the boundary of the material.

Characteristics of Edge and Surface States:
Edge and surface states typically exhibit linear dispersion relations near the Fermi level, indicating their Dirac-like nature. These states are localized near

the boundaries of the material and propagate along the edge or surface with well-defined momentum and spin textures. Spin-momentum locking, where the spin orientation is determined by the momentum direction, is a hallmark feature of edge and surface states in topological insulators.

2.6.1 Experimental Probes of Topological Properties

Experimental techniques play a crucial role in probing and characterizing the topological properties of materials, particularly topological insulators. Here, we explore several of these experimental techniques and discuss their strengths and limitations in studying these unique materials. Such experimental methods include angle resolved photoemission spectroscopy (ARPES), scanning tunneling microscopy/spectroscopy (STM/STS) and transport measurements.

1. **Angle-Resolved Photoemission Spectroscopy (ARPES):**
   - **Strengths:**
     - ARPES provides direct information about the electronic band structure, including the dispersion relation and Fermi surface.
     - It can identify the presence of surface or edge states in topological insulators by mapping out their momentum-resolved energy spectrum.
     - ARPES is sensitive to the spin texture of surface states, allowing for the determination of spin-momentum locking.
   - **Limitations:**
     - ARPES measurements are typically performed under ultra-high vacuum conditions, limiting the study to the surface electronic structure.

    - Surface sensitivity may obscure the observation of bulk topological properties, requiring careful interpretation of the experimental results.

2. **Scanning Tunneling Microscopy/Spectroscopy (STM/STS):**

   - **Strengths:**

     - STM/STS provides atomic-scale imaging and spectroscopy of the surface electronic structure of materials.
     - It can directly visualize the spatial distribution of surface states in topological insulators, including their energy dispersion and density of states.
     - STM/STS measurements can reveal the presence of topologically protected states and their spatial variations with high resolution.

   - **Limitations:**

     - STM/STS measurements are surface-sensitive and may not fully capture the bulk electronic properties of the material.
     - Surface roughness and sample preparation can introduce artifacts and affect the interpretation of the results.

3. **Transport Measurements:**

   - **Strengths:**

     - Transport measurements, including conductivity, Hall effect, and magnetoresistance, provide insights into the macroscopic electronic properties of materials.
     - They can reveal the presence of topologically protected surface or edge states through quantized conductance or anomalous Hall effect.

  - Transport measurements offer information about the electronic scattering mechanisms and mobility of charge carriers in topological insulators.

- **Limitations:**
  - Transport measurements may not directly probe the topological nature of the electronic states but rather their collective behavior.
  - The interpretation of transport data in topological insulators can be complex due to the presence of multiple electronic bands and scattering processes.

Experimental probes such as ARPES, STM/STS, and transport measurements play complementary roles in the study of topological insulators. While ARPES and STM/STS provide detailed information about the surface electronic structure and spatial distribution of surface states, transport measurements offer insights into the macroscopic electronic properties and topological features of the material. Several studies have employed ARPES to elucidate the existence of topologically protected surface states in materials such as Bi_2Se_3, Bi_2Te_3, and Sb_2Te_3 [15]. ARPES measurements have revealed the unique spin-textured Dirac surface states characteristic of topological insulators, confirming their nontrivial band topology and topological protection [16]. STM/STS studies on topological insulators have revealed the presence of topologically protected surface states with distinct electronic properties, such as linear dispersion and spin-momentum locking [17]. Furthermore, STS measurements have identified characteristic signatures of Dirac surface states, including the observation of quantized conductance plateaus and Andreev bound states in topological insulator-superconductor heterostructures [18]. Transport experiments have revealed the unique electronic transport phenomena associated with the topological surface states, such as the suppression of backscattering and the observation of quantum Hall effects without an external magnetic field (the quantum spin Hall effect) [19]. By studying the temperature, magnetic field, and gate voltage dependence of transport properties, researchers can elucidate the scattering mechanisms and quantum transport phenomena governing the behavior of topological insulators. Integrating multiple experimental techniques allows for a comprehensive understanding of the topological properties of materials and their potential applications in future technologies.

2.6.2 Optical Spectroscopy of Topological Insulators

Optical spectroscopy techniques provide valuable insights into the electronic structure and optical transitions in topological insulators. Studies employing techniques such as angle-resolved photoemission spectroscopy (ARPES), optical absorption spectroscopy, and magneto-optical spectroscopy have revealed the presence of distinct optical transitions associated with the topological surface states [20]. The optical conductivity of topological insulators exhibits characteristic signatures of the Dirac surface states, including a linear frequency dependence and strong optical absorption in the mid-infrared region [21]. Nonlinear optical effects in topological insulators have attracted considerable interest due to their potential for novel optoelectronic applications. The nonlinear optical response of topological insulators arises from the strong light-matter interactions facilitated by the spin-momentum locking of the surface states. Recent theoretical and experimental studies have explored nonlinear optical phenomena such as second-harmonic generation (SHG) and third-harmonic generation (THG) in topological insulator thin films and nanostructures [22]. These studies have demonstrated the potential of topological insulators for efficient nonlinear optical devices and all-optical signal processing. The unique optical properties of topological insulators have inspired the development of novel photonic devices with enhanced functionality and performance. Integrating topological insulators into photonic structures enables the manipulation and control of light at the nanoscale. For instance, the incorporation of topological insulator thin films in photonic waveguides and resonators offers opportunities for realizing low-loss photonic circuits and efficient light-matter interaction platforms [23]. Furthermore, the topological protection of surface states in topological insulators provides robustness against imperfections and disorder, making them promising candidates for photonic devices operating under harsh environmental conditions. While significant progress has been made in understanding the optical properties of topological insulators, several challenges and opportunities remain for future research. This dissertation presents a comprehensive optical investigation of two prominent topological insulators, Bismuth Selenide (Bi_2Se_3) and Antimony Telluride (Sb_2Te_3).

Chapter 3

3 METHODOLOGY AND EXPERIMENTAL TECHNIQUES

Already synthesized bulk crystals (synthesised by Bridgman method at Chimed in Moscow, Russia) of Bi_2Se_3 and Sb_2Te_3 in centimetre range were cleaved and optical reflectivity measured from the (001) plane. The samples were first characterized through resistivity measurements. Reflectivity was then measured at room temperature in the near-infrared to ultraviolet spectral ranges with a UV/Vis/NIR Perking Elmer Lambda 1050+ Spectrometer at the University of Dar es saalam, in Tanzania. The reflectivity measurements were extended down to the mid infrared range with the aid of Bruker 80 spectrometer at the Universität Stuttgart in Germany and In all the above reflectivity measurements, freshly evaporated gold mirrors served for reference measurements. Figure 1 shows pictures of samples used in the current investigations.

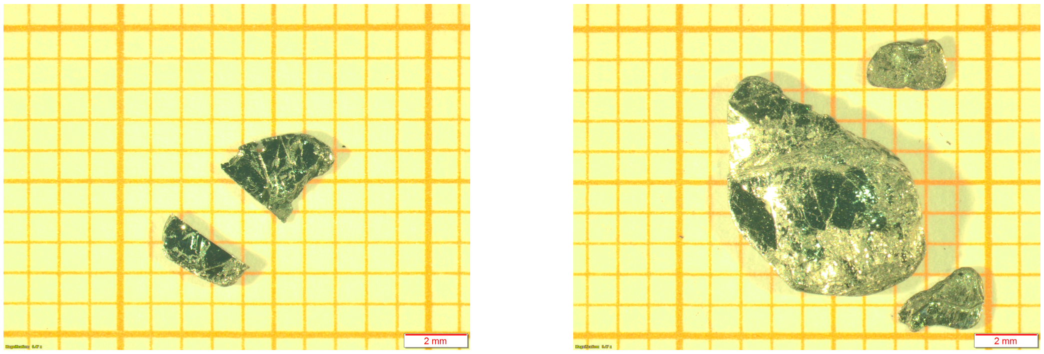

(a) Bi_2Se_3 single crystals

(b) Sb_2Te_3 single crystals

Figure 1: Investigated single crystals

3.1 Resistivity

Electrical transport experiments were carried out by Hall bar geometry measurement system. The Hall bar geometry is specifically designed for Hall effect and electrical transport measurements. This configuration is widely used due to its simplicity and accuracy in determining material properties such as carrier density, mobility, and resistivity. The well-defined geometry ensures precise control over current flow and voltage measurements, reducing errors caused by irregular sample shapes or non-uniform current distributions. The sample was fabricated in a rectangular "bar" shape with well-defined dimensions (length, width, and thickness) to simplify resistivity and Hall effect calculations. Mechanical cutting method was used with the aid of a microscope to shape the sample. six contacts were placed on the sample to facilitate both longitudinal and transverse measurements, four of which measured the longitudinal resistance and two measured the transverse resistance.

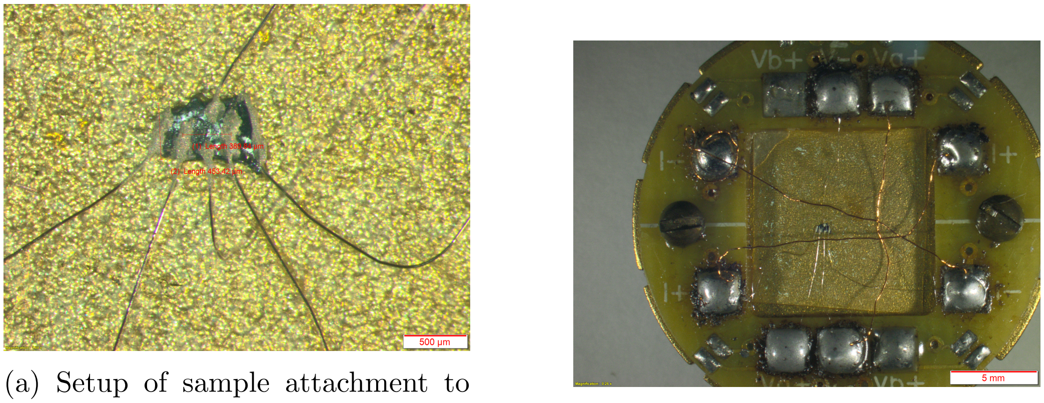

(a) Setup of sample attachment to the 6 wires

(b) 6 probe configuration setup

Figure 2: Hall Bar geometry measurement setup

3.2 UV/Vis/NIR Perking Elmer Lambda 1050+ Spectrometer

The Perkin Elmer Lambda 1050+ UV/Vis/NIR spectrometer is a sophisticated instrument used for analyzing the optical properties of materials across a wide spectral range, spanning ultraviolet (UV), visible (Vis), and near-infrared (NIR) wavelengths. Calibration of UV/Visible/NIR perking Elmer Lambda 1050+ spectrometer was one of the objectives of the current research. In order to calibrate the Perkin Elmer lambda 1050+ spectrometer, reflectivity data was collected for the sample at the University of Dar Es Salaam and data obtained at room temperature was compared with the data obtained at 300K by the Bruker vertex 80 Spectrometer.

Figure 3: Perkin Elmer Lambda 1050+ Spectrometer

Detailed guide on how to obtain reflectivity data from the Perkin Elmer Lambda 1050+ spectrometer can be found in the user manual [24]

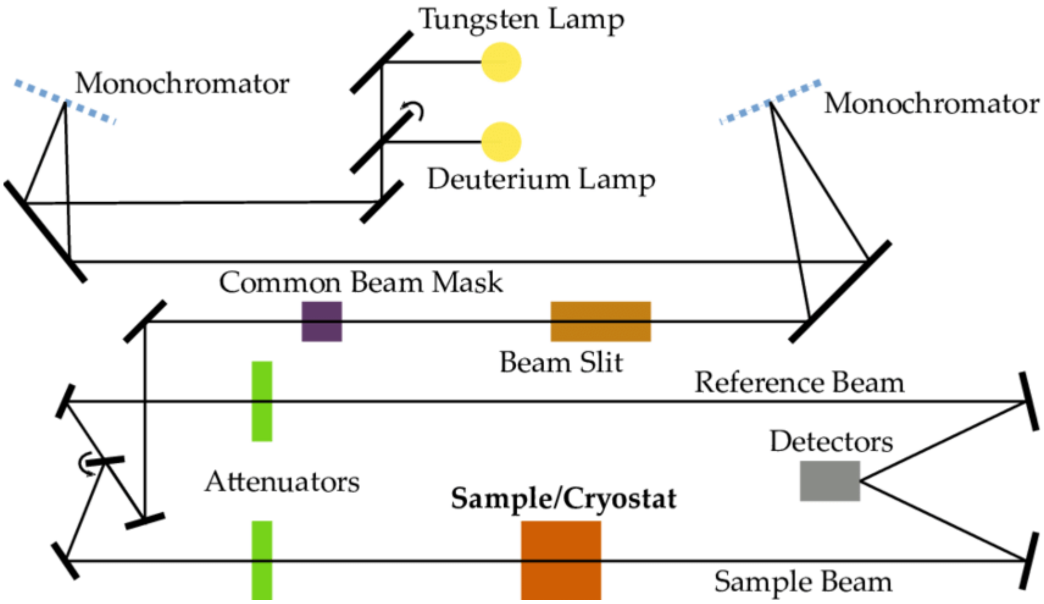

Figure 4: Optical layout of the Perkin Elmer Lambda 1050+ Spectrometer for reflectivity measurements

3.3 Infrared Spectroscopy

Infrared radiation spans a section of the electromagnetic spectrum having wavenumbers from roughly 10 to 13,000 cm^{-1} [25]. Infrared spectroscopy [26] [27] covers a wide range of frequencies. Depending on the frequency range of interest, different combinations of sources, optical windows, filters beam splitters, detectors etc are used. To measure the frequency ranges used in this dissertation, the Bruker Tensor 80 FTIR (Fourier Transform Infrared) spectrometer was utilized for conducting infrared spectroscopy, a technique used to analyze the molecular composition and structure of materials based on their interaction with infrared radiation. Here's how the Bruker Tensor 80 was typically used for this purpose:

Instrument Setup: The Bruker Tensor 80 is equipped with a variety of accessories and modules to accommodate different types of samples and ex-

Figure 5: Bruker vertex 80 Spectrometer

perimental requirements. Users select the appropriate sampling accessory depending on whether they are analyzing solids, liquids, gases, thin films, or other sample types.

Instrument Calibration: Prior to analysis, the spectrometer was calibrated by using freshly evaporated gold mirrors as reference to ensure accurate measurement and calibration of the instrument parameters such as wave number, spectral resolution, and intensity. Details on how data is collected, stored and retrieved can be obtained from the following user manuals provided herein [28]

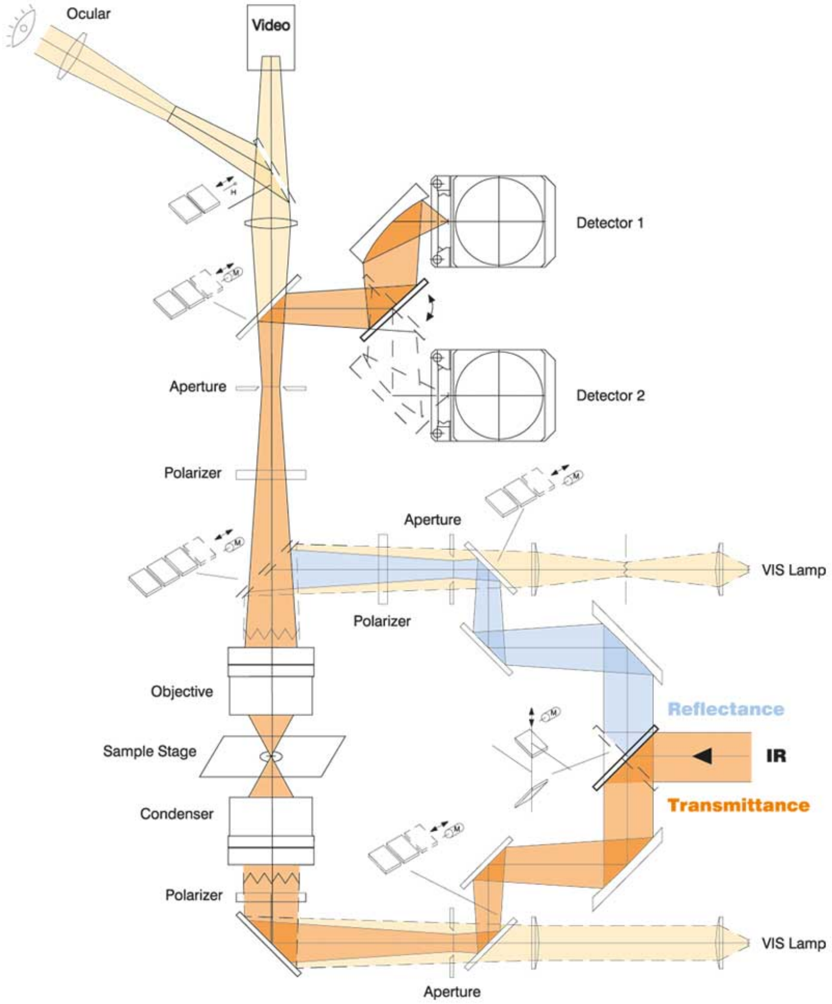

Figure 6: Optical layout of the Bruker vertex 80 Spectrometer

Chapter 4

4 DATA ANALYSIS

To investigate a material by optical reflectivity means reflectivity data needs to be collected over a wide range of frequencies using different radiation sources, optical windows filters and detectors [29]. Hence, one needs to know how to handle such data collected from these infrared spectroscopy independent measurements which is the aim of this chapter. Firstly, the measured raw data at each temperature needs to be merged for different frequencies i.e, FIR, MIR, NIR and room temperature NIR-visible ellipsometry. Secondly, extrapolations both at low and high frequencies are made after which Kramers-Kronig analysis is performed to obtain the optical conductivity and dielectric constant from the reflectivity data. The optical conductivity obtained from Kramers-Kronig analysis and the merged reflectivity data are then fitted using Wasf program with Drude-Lorentz contributions. The fitting to the reflectivity is then used for smoothing of the measured reflectivity. Finally, second Kramers-Kronig analysis is applied on the smoothed reflectivity and the obtained smoothed conductivity are then used for calculating other fundamental properties which are of importance in as far as optical investigation of materials in concerned. Underneath here are the explanations of the various steps involved in data handling.
The optical conductivities of Sb_2Te_3 and Bi_2Se_3 were analyzed using Extended Drude Analysis (EDA).

4.1 Data Merging and Extrapolation

The reflectivity data from Far-Infrared (FIR), Mid-Infrared (MIR), and Near-Infrared (NIR) spectroscopy were combined and extrapolated from 500 cm^{-1} to 1 cm^{-1} using a polynomial extrapolation method as shown in Figure 7.

At high frequencies ($\omega \to \infty$), reflectivity goes from zero. This was applied to both samples and for all temperatures.

$$\text{Reflectivity} = \text{FIR} + \text{MIR} + \text{NIR} \tag{25}$$

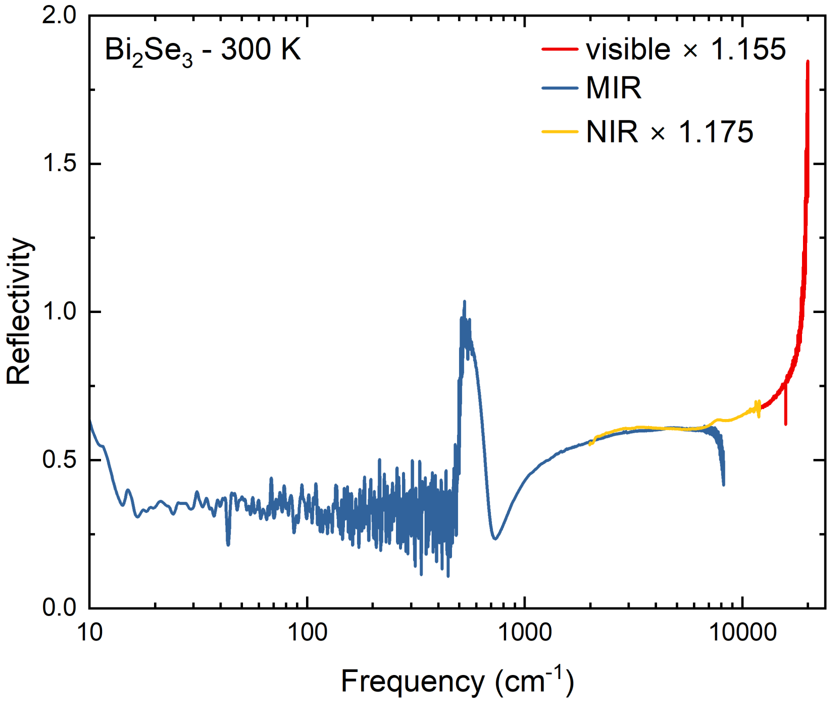

Figure 7: Merged data for Bi_2Se_3 at 300K

4.2 Kramers-Kronig Analysis

Kramers-Kronig transformation was performed on the extrapolated data to obtain the complex dielectric function $\epsilon(\omega) = \epsilon_1(\omega) + i\epsilon_2(\omega)$. The merged and extrapolated data was loaded in the Kramers-Kronig program after which zeroes were removed to avoid run time errors and the program was then run. The real and imaginary part of the complex conductivity σ_1 and (σ_2) was then calculated respectively.

$$\epsilon(\omega) = \frac{1}{\pi}\mathcal{P}\int_{-\infty}^{\infty}\frac{\sigma(\omega')}{\omega' - \omega}d\omega' \tag{26}$$

During this process, two restrictions of practical importance were adhered to i.e. data covered a wide spectral range and the sample was be opaque

4.3 Wasf fitting of reflectivity and conductivity

After Kramers-Kronig analysis, the merged extrapolated reflectivity and the calculated conductivity were fed into the Wasf program where they were fitted with various Drude-Lorentz components as shown in Figure 8.

Figure 8: WASF fit

The reflectivity and conductivity spectra were fitted with one Drude and three Lorentz oscillators. The two fitting parameters for the Drude contributions are damping or scattering rate in cm^{-1} and dc conductivity in Ω^{-1}cm^{-1} at a given temperature. The plasma frequency for the Drude component was calculated automatically by the program on inserting the fitting parameters for the Drude. For Lorentzian fit, the fitting parameters included delta epsilon, the central frequency of the oscillator in the cm^{-1} and the damping rate in cm^{-1}. The oscillator strength or the plasma frequency for the Lorentz fit was also readily calculated as the case was with Drude fittings.

4.4 Smoothing of Reflectivity Data

The fitted reflectivity data was exported to origin program and used for smoothing of the experimental reflectivity data. The data in the normal conducting state was smoothed using the equation:

$$R_{smoothed} = \frac{(R_{experimental}) \times 1 + (R_{fitted} \times 2)}{3}$$

where R is the reflectivity.

In addition to smoothing using the above equation, strange noise in the spectra such as that due to CO_2 around 2200 cm^{-1} was also removed. Figure 9 shows the smoothed data compared to the merged measured data. From this Figure one can see that the smoothed data agreed with the measured data very well. Using the smoothed reflectivity data free from noise, a second Kramers-Kronig analysis was done and smooth conductivity obtained which was later used for spectral weight calculations and extended Drude analysis.

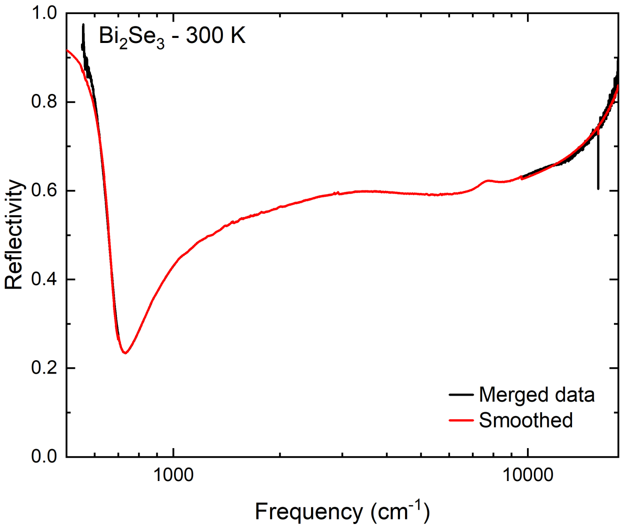

Figure 9: Smoothed data for Bi_2Se_3 at 300K

4.5 Spectral weight analysis

The spectral weight (SW) was calculated by integrating the optical conductivity $\sigma(\omega)$ over the frequency range as confirmed in [30].

$$SW(\omega_c) = \frac{120}{\pi} \int_0^{w_c} \sigma_1(\omega) d\omega = \frac{4\pi n e^2}{m} = \omega_p^2 \tag{27}$$

4.6 Extended Drude Analysis

The optical conductivity $\sigma(\omega)$ was extracted from $\epsilon(\omega)$ and fitted with the Drude model.

$$\sigma(\omega) = \frac{\omega_p^2}{4\pi} \frac{1}{1/\tau - i\omega} \tag{28}$$

Parameters extracted:

	Parameter
1	Scattering rate($1/\tau$)
2	Normalized Effective mass (m^*)

Table 2: Extracted parameters from Extended Drude Analysis

Chapter 5

5 RESULTS PRESENTATION AND DISCUSSION

In this dissertation, two samples i.e Bi_2Se_3 and Sb_2Te_3 were investigated and results herein presented.

5.1 RESULTS AND DISCUSSION FOR ANTIMONY TELLURIDE (Sb_2Te_3)

5.1.1 Resistivity

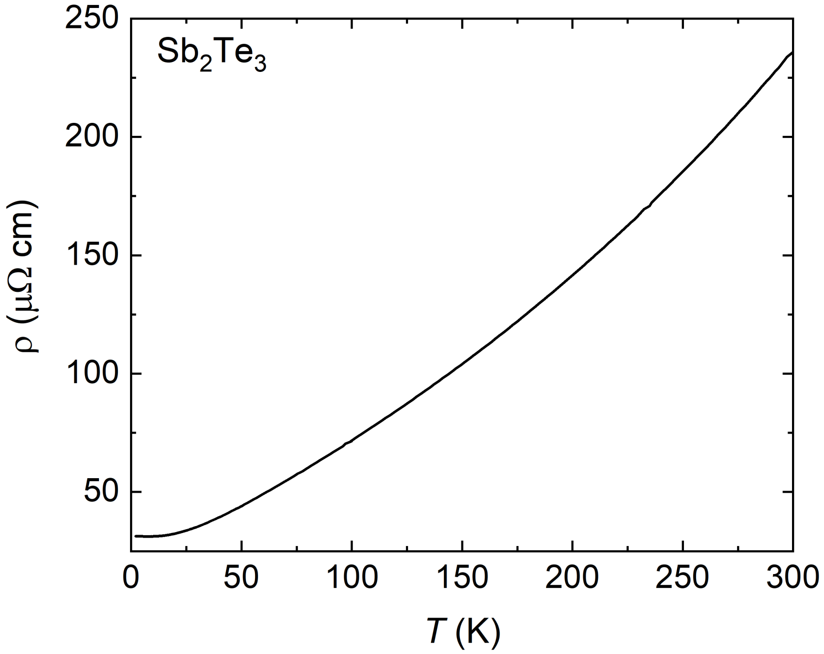

Figure 10: Resistivity of Sb_2Te_3 at varying temperatures

Figure 10 shows the temperature dependence of the resistivity of the Sb_2Te_3

sample crystal. In the measurements, a good metallic behavior, i.e, a decreasing resistivity with decreasing temperature is found. A residual resistivity ratio (RRR), i.e., $\frac{\rho(300K)}{\rho(2K)}$ of 7.51 is obtained in the current investigation. This RRR is somewhat higher than 7.1354 reported in Ref. [31] . The higher RRR value is attributed to a more pure sample.

5.1.2 Reflectivity

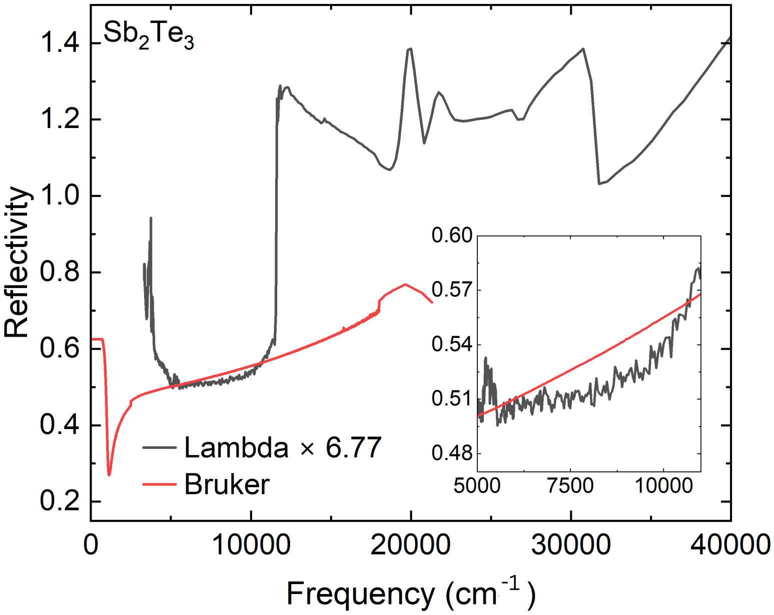

Figure 11: Reflectivity measurements of Sb_2Te_3 as obtained using the perkin Elmer lambda 1050+ spectrometer compared to the Bruker Vertex 80 spectrometer data.

From the calibration plot in Figure 11, the data had a huge mismatch and did not fit into the Calibration curve. Only a portion from 5000 to 12000 cm^{-}1 agreed with the standard measured Stuttgart data after multiplying it by a factor of 6.77. Below and above this range, the data obtained from the University of Dar-Es-Salaam was found not to be reliable. The mismatch could be due to the compromise made to the Perkin lambda 1050+ spectrometer which had no sample holders for measuring reflectivity of small samples and as such improvision was made but the alignment of the sample with the beam may not have been perfect.

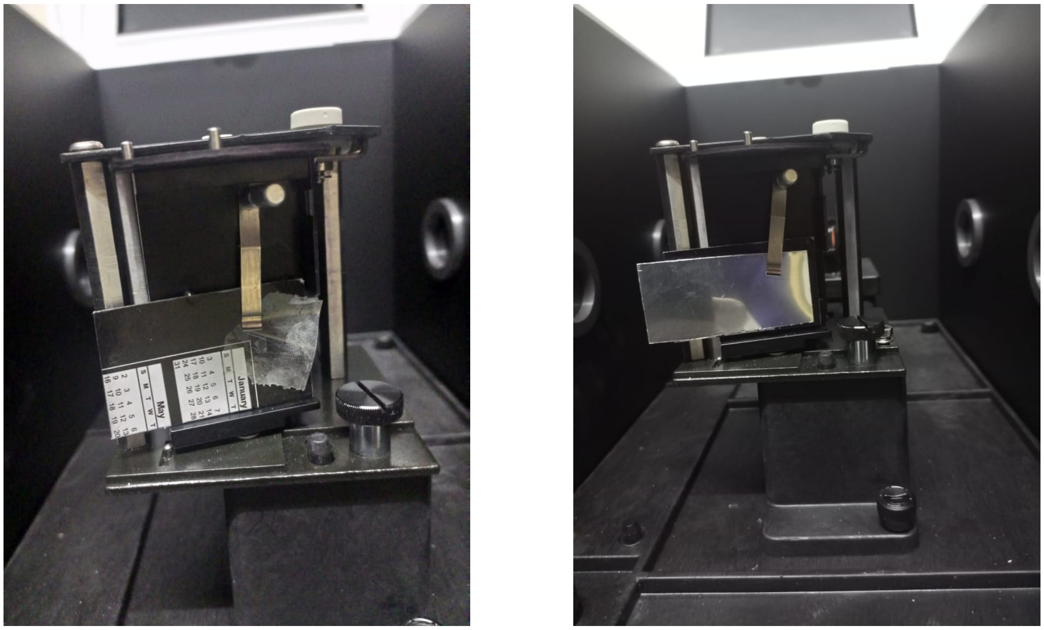

(a) Experimental setup with Improvised sample holder

(b) Experimental setup with gold mirror for calibration of parameters

Figure 12: Improvision of experimental setup due to lack of sample holders

The other reason could have been due to the fact that the experiment was not conducted in a dark room and as a result, the light rays from the room could have interfered with the reflectivity measurements.

The data at different temperatures was then collected further and at varying temperatures using the Bruker vertex 80 spectrometer, which is one of the standard equipment for measuring reflectivity for small samples.

Figure 13 shows the graph of reflectivity of Sb_2Te_3 for frequencies ranging from 500 to 18 000 cm^{-1} for temperatures ranging from 13 K to 300 K respectively. Reflectivity for frequencies below 700 cm^{-1} portrays constant

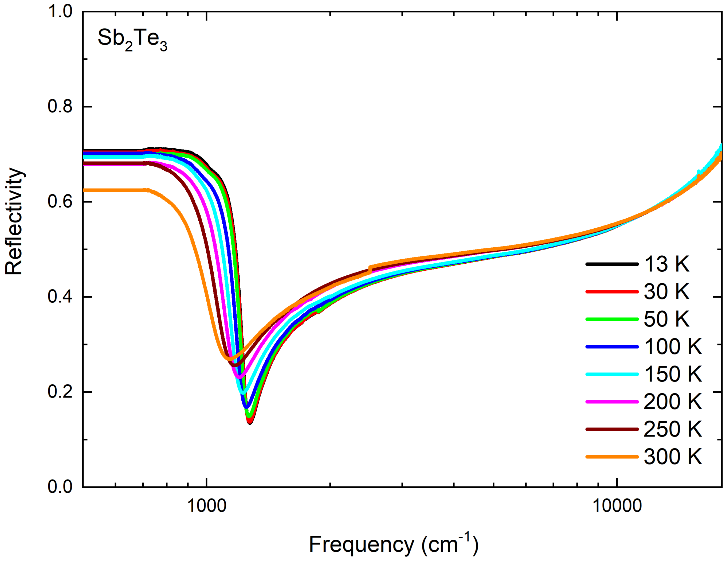

Figure 13: Reflectivity for Sb_2Te_3 at different temperatures

behavior for all temperatures due to the fact that at low frequencies, Phonon modes do not significantly change with temperature due to the stability of these phonon modes in Sb_2Te_3. For all temperatures, the reflectivity decreases with increasing frequency up to about 1200 cm^1, beyond which it increases slightly with further frequency increase. The increase above 1200 cm^{-1} is attributed to interband transitions. The reflectivity curves for different temperatures cross each other in the frequency range 1100 to 1300 cm^{-1}. This behavior is a clear sign of spectral weight transfer to low frequencies on cooling, leading to Drude like contributions at low frequencies narrowing and sharpening on cooling. In particular, at lower temperatures, the electrons tend to occupy lower energy states, possibly leading to changes in the electronic bandgap (a bandgap is evident above 1000 cm^{-1} as seen in $\sigma_1(\omega)$ going to zero) or dispersion relation. These changes in the band structure can influence the plasma frequency and shift the plasma minimum to higher frequencies. At higher frequencies, interband transitions above 10 000 cm^{-1}, reflectivity show no temperature dependence.

5.1.3 Conductivity

By carrying out Kramers Kronig analysis on reflectance data, the real and imaginary parts of conductivity were obtained, i.e

$$\sigma(\omega) = \sigma_1(\omega) + i\sigma_2(\omega) \tag{29}$$

where σ_1 and σ_2 are real and imaginary parts of the complex conductivity, respectively. These were obtained over a broad range of frequencies and different temperatures for Sb_2Te_3.

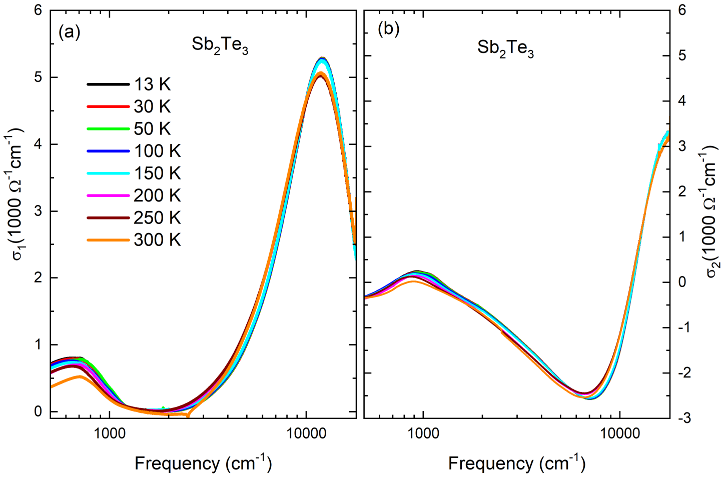

Figure 14: Real(a) and Imaginary(b) parts of Conductivity for Sb_2Te_3 at different temperatures

From Figure 14, it can be seen that the real part of optical conductivity at low frequencies in the normal state decreases with an increase in temperature and shows well defined Drude-like modes. The Drude peak decreases with increasing temperatures as seen in the Figure 14(a). The decrease in the real part of optical conductivity (σ_1) at low frequencies with increasing temperature can be attributed to the scattering of charge carriers. The FIR band also grows with a decrease in temperature and such FIR band has been observed in Pr_2CuO_4 [13]. As temperature rises, lattice vibrations become more pronounced. The Drude model can explain this behavior. It considers the collective behavior of charge carriers in a material and their response to an external electric field. The Drude model predicts that the real part of optical conductivity at low frequencies is proportional to the carrier mobility and carrier concentration. In the case of Sb_2Te_3, the decrease in carrier mobility due to scattering by phonons dominates, leading to a reduction in σ_1 with increasing temperature. However, at higher frequencies, beyond 2000 cm^{-1}, it is observed that the prediction of the Drude theory according to which the optical conductivity should drop down to zero as $\frac{1}{w^2}$ does not hold but instead, the conductivity begins to rise with increasing frequency, going to a maximum and a NIR band is observed. The NIR band is attributed to interband transitions. The appearance of a NIR band in its optical conductivity spectrum could be attributed to transitions between electronic energy levels within the material known as interband transitions and the results are in agreement with those by Adhikari [32]. The difference comes from the fact that the Drude theory does not take into account the interband transitions. The interband threshold may be due to excitation of electrons from the valence band into higher unoccupied levels or from the valence band into unoccupied levels in the conduction band. The rise in conductivity with frequency is due to the fact that the increase in energy ($E = hf$) enhanced the electron mobility and subsequently the conductivity value. In Sb_2Te_3 no phonon modes are observed. A decrease after 10,000 cm^{-1} is observed in the real part of optical conductivity which is due to interband transitions. The electrons transition from the valence band to higher energy bands, thereby reducing the number of free carriers contributing to conductivity. The real part of the optical conductivity of Sb_2Te_3 for all temperatures ranging from 13 K to 300 K were inspected and only extreme temperatures recorded so as to look for linearity dependence in any frequency range. Some sort of linearity in this particular sample could not be seen clearly as shown in Figure 15 where plots of 13 K and 300 K (lowest and highest measured conductiv-

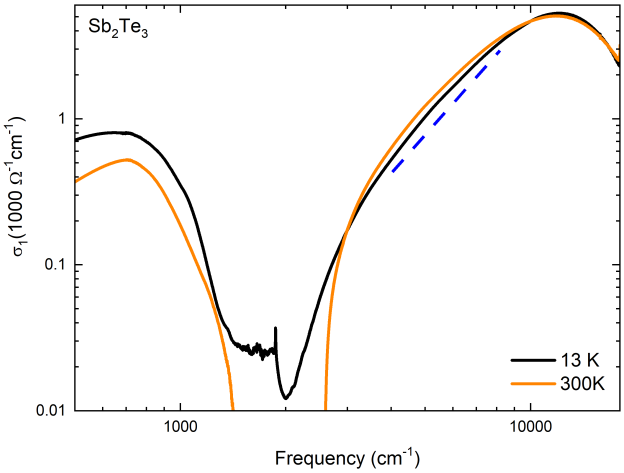

Figure 15: Sb_2Te_3 showing no linearity for Conductivity at 13 and 300 K as can be seen by the departure of conductivity curves from the dashed line(linearity line)

ity temperature curves) are shown, compared with the linearity line(dashed line). No linearity dependence is evident for Sb_2Te_3
Zhukova et al [33] ascribes this linearity to the cumulative effect of transitions between the bands with complex dispersion hence absence of linearity in the frequency dependence of optical conductivity for Sb_2Te_3 points to the absence of cumulative effect of transitions in the sample.
For the imaginary part of the optical conductivity (σ_2), the conductivity first increases with frequency and begins to decrease thereafter. The frequency at which a maximum in $\sigma_2(\omega)$ is reached is ascribed to the scattering rate as inferred from the theory. From Figure 14(b), the scattering rate for Sb_2Te_3 is about 1000 cm^{-1}. Above 10,000 cm^{-1}, the rise in the conductivity is evidence of a rise in absorption due brought about by the interband transitions.

5.1.4 Extended Drude analysis

The extended Drude analysis gives a description or know how of the effect of many body interactions on the itinerant behaviour of charge carriers. The temperature dependence of the effective mass and the scattering rate are plotted in Figure 16(a) and 16(b) respectively.

The effective mass up to 1000 cm^{-1} is observed to increase with increase in frequency at all temperatures, a departure from the simple Drude response which predicts a constant effective mass and this typically indicates the presence of strong electron-phonon coupling in the material often associated with enhanced electron-phonon scattering, which can have several consequences on the material's electronic properties, such as the enhanced electrical resistivity.

Another notable feature is that the normalised effective mass gets stronger with a decrease in temperature below 1000 cm^{-1} and this behavior is a signature of correlation effects. The mass enhancement factor then decreases rapidly with increasing frequency from 1000 to 1500 cm^{-1}, suggesting the emergence of a specific electronic behavior related to the material's electronic band structure and scattering mechanisms. The mass enhancement factor then approaches zero at frequencies above 1500 cm^{-1} as a consequence of the limitations of the electron-phonon interaction model used to describe the material's behavior. In condensed matter Physics, the electron-phonon interaction is typically described using the Migdal-Eliashberg theory, which assumes that the electron-phonon coupling is weak and perturbative [34]. However, this assumption breaks down at high frequencies, where the coupling becomes stronger and non-perturbative effects come into play. At high frequencies, the electron-phonon coupling strength becomes too strong for the perturbative model to accurately describe the interactions between electrons and phonons. As a result, the mass enhancement factor, which is a measure of the strength of the electron-phonon interaction, starts to decrease and eventually approaches zero.

From Figure 16(a), it can be seen that the scattering rate increases continuously and monotonically with frequency upto 1200 cm^{-1} beyond which it decreases monotonically with frequency without any saturation resulting in a contradiction to the electron phonon-scattering theory which predicts a constant frequency independent scattering rate above 500 cm^{-1} [35] and this absence of saturation seems to suggest that in addition to electron-phonon scattering, there are other scattering channels which may arise from electronic and spin correlations.

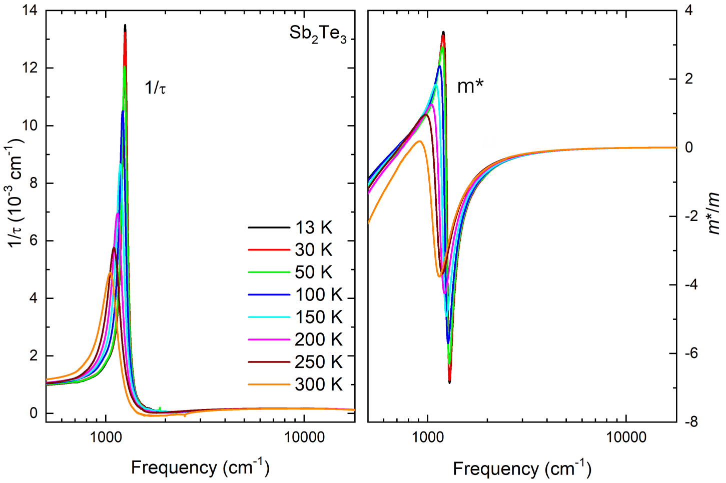

Figure 16: Scattering rate and mass enhancement factor for Sb_2Te_3

5.2 RESULTS AND DISCUSSION FOR BISMUTH SELENIDE (Bi_2Se_3)

5.2.1 Resistivity

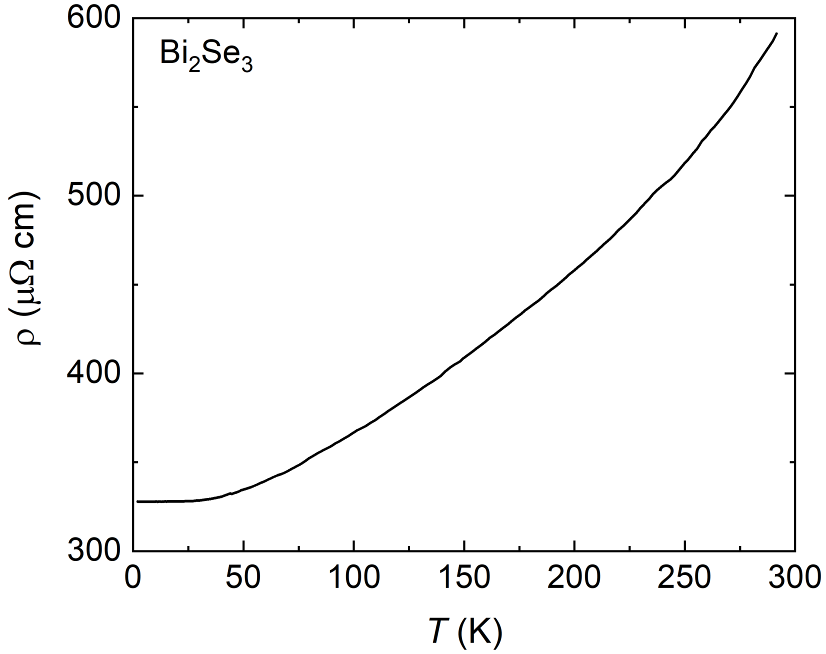

Figure 17: Resistivity of Bi_2Se_3 at varying temperatures

The temperature dependence of the resistivity of the Bi_2Se_3 crystal is plotted in Figure 17 and in the measurements, a good metallic behavior, i.e, a decreasing resistivity with decreasing temperature is found. A residual resistivity ratio (RRR), i.e., $\frac{\rho(291.7K)}{\rho(2K)}$ of 1.80 is obtained in the current investigation. This RRR is somewhat higher than 1.74 reported in Ref. [36]. The higher RRR obtained here indicates high crystalline quality of the current sample.

5.2.2 Reflectivity

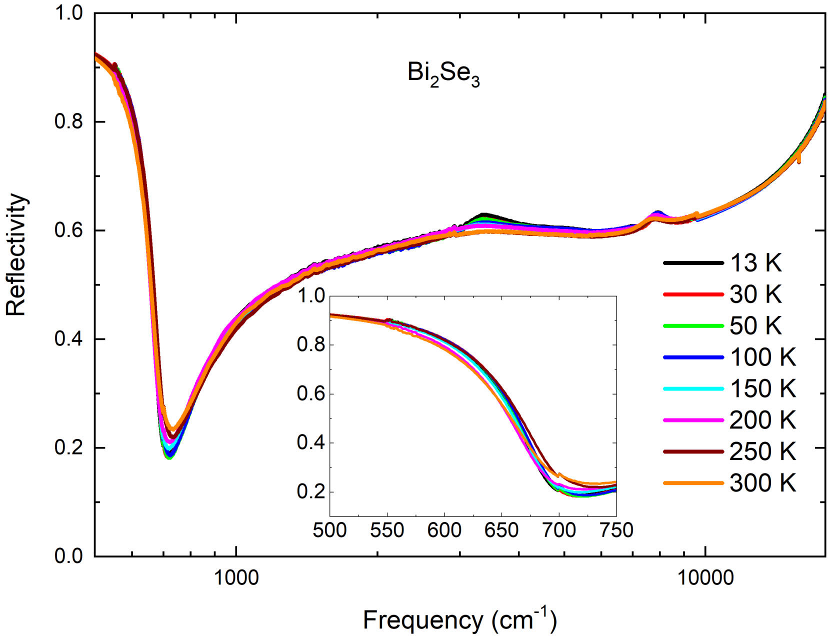

Figure 18: Reflectivity in Bi_2Se_3 at varying temperatures

Figure 18 shows the graph of reflectivity of Bi_2Se_3 for frequencies ranging from 500 cm^{-1} to 18,000 cm^{-1} for temperatures ranging from 5 to 300 K respectively, of which all the temperatures show metallic behavior and is observed to have good metallic behavior due to the presence of a plasma like feature. The plasma-like feature, which refers to the Dirac surface states, indicates metallic behavior because these surface states behave like a 2D electron gas with linear energy dispersion. In a conventional metal, the energy of electrons near the Fermi level is also linear with momentum, leading to a metallic behavior with high electrical conductivity. In Bi_2Se_3, the presence of Dirac surface states allows electrons to move freely along the surface with minimal scattering. This linear energy-momentum relationship results in a high density of states at the Fermi level and contributes to its metallic behavior. At zero frequency, all the spectra of reflectivity approach absolute reflectance. In Bi_2Se_3, the plasma is observed to soften (shifting to lower frequencies) as temperature decreases as also observed in references [37] and [38], even though it was not discussed, and was seen to be around 380 to 420 cm^{-1}. The spectra of reflectivity in Bi_2Se_3 seems to approach absolute reflectance at zero frequency due to the presence of the plasma-like feature or Dirac surface states. At zero frequency (DC limit), the incident photons have low energy or very long wavelengths. In this limit, the electronic response of the material is dominated by its low-energy excitations, which in this case are the Dirac surface states. The Dirac surface states in Bi_2Se_3 have a linear energy dispersion, meaning their energy increases linearly with momentum. As the incident photons have very low energy, they interact with these linearly dispersing surface states, leading to a strong and coherent electron-photon interaction. This interaction results in efficient coupling of the photons to the surface states, leading to a high reflectivity and approaching absolute reflectance at zero frequency. In simpler terms, at very low energies, the photons efficiently interact with the unique surface electronic states of the material, causing the material to reflect almost all incident light. A direct band gap between 3000 and 4000 cm^{-1} is seen and was also observed in [39]. This shows the region where the crystal momentum of electrons and holes remains the same in the conduction band and the valence band, and in this region, an electron can directly emit a photon, and the recombination process is much more efficient in this material as a result. In this region of the direct bandgap, the peak increases with a decrease in temperature. From 600 to 750 cm^{-1}), reflectivity curve as a function of temperature is seen to cross each other, which is a clear sign of scattering rate increasing with increase in temperature and vice versa (scattering rate becoming smaller on cooling).

The hump like structures observed in the range 3000 to 10,000 cm^{-1} are due to interband transitions [40] and in this case, the MIR shows temperature dependence while the NIR-Visible interband transition shows no temperature dependence. Interband transitions in the near-infrared (NIR) region of the graph of reflectivity and frequency typically do not show strong temperature dependence due to the nature of these transitions and the energy involved. Interband transitions refer to the absorption of photons by electrons to move from the valence band to the conduction band, promoting them across the band gap. In the NIR region, the energy of the incident photons is relatively low compared to the band gap energy of the material. At room temperature and in the NIR region, most materials, including semiconductors like Bi_2Se_3, have well-defined energy bands and a fixed band gap. The energy of the photons involved in NIR interband transitions is much smaller than the thermal energy at room temperature. As a result, the transition probabilities remain relatively constant and do not show significant temperature dependence. However, it's worth noting that while the interband transitions themselves may not show strong temperature dependence in the NIR region, the overall reflectivity and absorption characteristics of the material can still be influenced by other temperature-dependent factors, such as lattice vibrations, thermal expansion, and carrier scattering processes. These factors may lead to subtle changes in the overall reflectivity spectrum with temperature, but the interband transitions themselves remain relatively temperature-independent in the NIR region. Furthemore, reflectivity was measured at the University of Dar es salaam at room temperature using the Perkin Elmer Lambda 1050+ spectrometer. Figure 19 shows the reflectivity of Bi_2Se_3 at room temperature measured in Dar es Salaam, compared to the one measured at the University of Stuttgart using the Bruker 80 at 300 K. One can clearly see that data from Dar es Salaam only agrees with data from Stuttgart in the frequency range 6000 to 8500 cm^-1 window. In Figure 19, the data collected over the range of 6000 to 8500 cm^{-1} compared very well with the data from Stuttgart, even though the reflectivity from Dar Es Salaam was lower and only matched with data from Stuttgart after being multiplied by a factor of 1.25, beyond which the data equally had a huge mismatch and did not fit into the Calibration curve. The mismatch could be

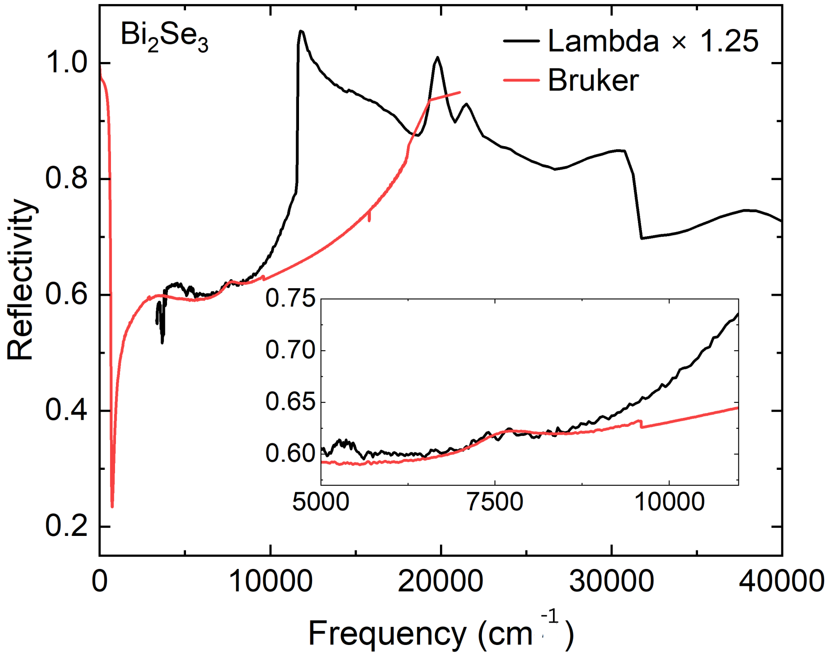

Figure 19: Reflectivity measurements at 300 K for Bi_2Se_3 as obtained using the perkin Elmer lambda 1050+ spectrometer compared to the Bruker Vertex 80 spectrometer data

due to the challenges stated in Section 5.1.2.

5.2.3 Conductivity

By using Krammers Kronig analysis on reflectance data, the real and imaginary parts of conductivity were obtained over a broad range of frequencies and different temperatures for Bi_2Se_3.

From Figure 20(a), it can be seen that the real part of optical conductivity at low frequencies decreases with an increase in frequency and shows well defined Drude-like modes. The Drude peak in the sample increases with increasing temperature. As temperature increases, the carrier density may increase, especially if there is thermal excitation of carriers from impurity states or the surface states into the conduction band. This could enhance the Drude peak,

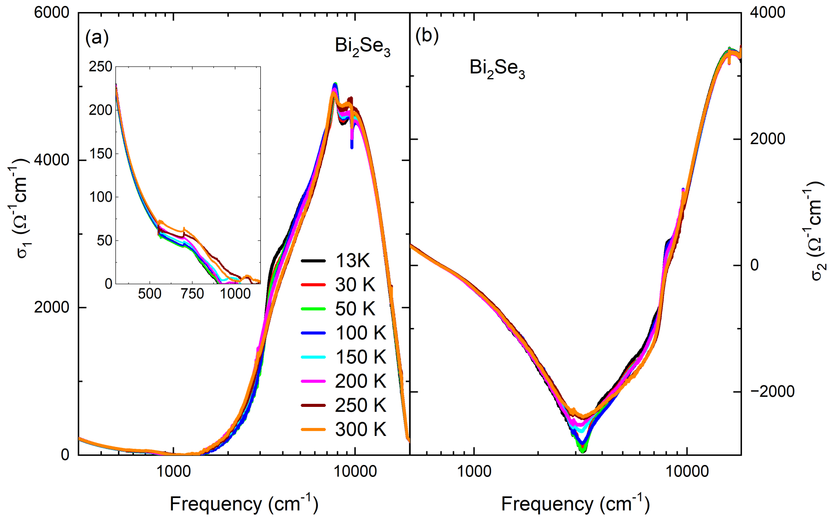

Figure 20: Conductivity of Bi_2Se_3 at various temperatures

as more charge carriers contribute to the optical conductivity. A hump-like structure is observed between 3000 to 5000 cm^{-1} which is brought about due to spectral weight transfer to higher frequencies on cooling, thereby leading to the observed interband transition of Bi_2Se_3, which is a hump-like structure at frequency ranges of 6000 to 9000 cm^{-1}. In the figure of conductivity for the sample, it is seen that at very high frequencies, there is a decrease in conductivity and this is due to the fact that at high frequencies, the ions oscillate so fast that the net ionic motion along a particular direction is smaller than that in the presence of a static or low frequency field. A closer look at the real part of conductivity, $\sigma_1(\omega)$, shows conductivity to be linear in frequency over a broad range of 1500 to 3000 cm^{-1} as seen in Figure 21. This linearity strongly suggests the presence of three dimensional linear electronic bands with band crossings or rather nodes near the chemical potential and according to calculations made by Pronin et al [41], it was reported that the observed nearly linear $\sigma_1(\omega)$ originated as a cumulative effect from transitions near the tripple points as seconded by F.Hutt et al, 2018 [42].

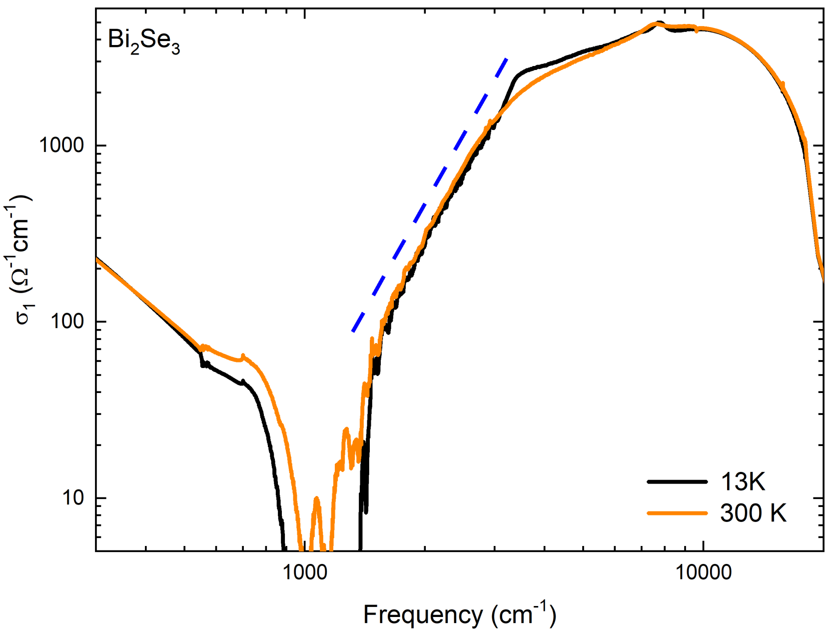

Figure 21: Bi_2Se_3 showing linearity in conductivity at 13 and 300 K

For the imaginary part of the optical conductivity (σ_2), the conductivity first increases with frequency and begins to decrease thereafter. The frequency at which a maximum in $\sigma_2(\omega)$ is reached in the normal state is due to the scattering rate as inferred from the theory[43, 44]. No maximum is observed in σ_1 below 3000 cm^{-1} at all temperatures. This means the scattering rate is below 500 cm^{-1} for all measured temperatures.

5.3 Extended Drude analysis

Having had established that the extended Drude analysis gives a description of the effect of many body interactions on the itinerant behaviour of charge carriers and having the scattering rate $\frac{1}{\tau}$ and the normalised effective mass obtained from the analysis using equations 16 and 17, in a like manner as the previous sample, the temperature dependence of the effective mass and the scattering rate are plotted in Figure 22(a) and 22(b) respectively.

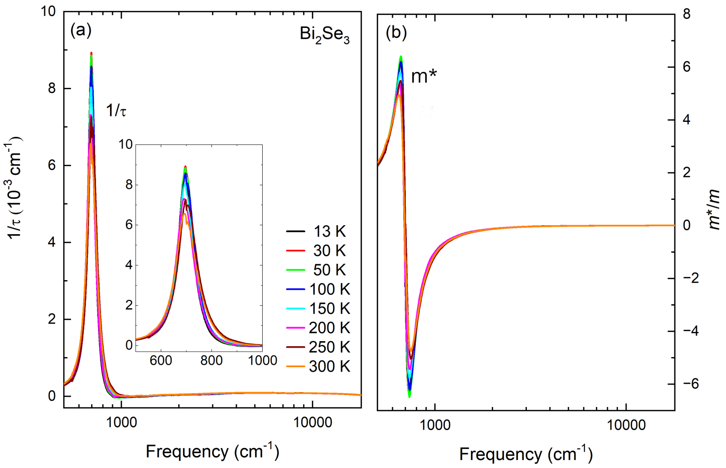

Figure 22: Scattering rate(a) and Mass enhancement factor(b) for Bi$_2$Se$_3$

At all measured temperatures, the effective mass up to 1000 cm^{-1} is observed to increase with increase in frequency which is a departure from the simple Drude response which predicts a constant effective mass and this typically indicates the presence of strong electron-phonon coupling in the material. Electron-phonon coupling refers to the interaction between electrons and lattice vibrations (phonons) in a solid. In this context, at lower frequencies (up to 1300 cm^{-1}), the lattice vibrations significantly affect the behavior of electrons, leading to an increase in the effective mass of the electrons. This phenomenon is known as "mass enhancement" because the electrons behave as if they have a larger mass due to their strong coupling with phonons. The increase in the mass enhancement factor is often associated with enhanced electron-phonon scattering, which can have several consequences on the material's electronic properties, such as the enhanced electrical resistivity as the increased scattering of electrons by phonons can hinder the flow of charge carriers, resulting in higher electrical resistivity. Another consequence is the decreased electronic mobility as strong electron-phonon coupling can reduce the mobility of charge carriers, thereby impacting their ability to move through the crystal lattice. Additionally, the normalised effective mass enhancement gets stronger with a decrease in temperature and this behavior is a signature of correlation effects. The mass enhancement factor then decreases rapidly with increasing frequency from 1000 to 1050 cm^{-1}, suggesting the emergence of a specific electronic behavior related to the material's electronic band structure and scattering mechanisms. Several factors may contribute to this phenomenon including the band structure effects since the electronic band structure of a material plays a crucial role in determining the effective mass of electrons. At certain frequency ranges, changes in the band structure can lead to modifications in the effective mass, resulting in a rapid decrease in the mass enhancement factor. Another factor could be the transition between energy bands as the decrease in the mass enhancement factor could be associated with a transition between different energy bands and as the frequency changes, the electrons may shift from one energy band to another, leading to variations in their effective mass. The mass enhancement factor then approaches zero at frequencies above 1050 cm^{-1} as a consequence of the limitations of the electron-phonon interaction model used to describe the material's behavior. In condensed matter Physics, the electron-phonon interaction is typically described using the Migdal-Eliashberg theory, which assumes that the electron-phonon coupling is weak and perturbative [34]. However, this assumption breaks down at high frequencies, where the coupling becomes stronger and non-perturbative effects come into play. At high frequencies, the electron-phonon coupling strength becomes too strong for the perturbative model to accurately describe the interactions between electrons and phonons. As a result, the mass enhancement factor, which is a measure of the strength of the electron-phonon interaction, starts to decrease and eventually approaches zero.

from figure 22(b), it can be seen that the scattering rate increases continuously and monotonically with frequency upto 700 cm^{-1} beyond which it decreases monotonically with frequency without any saturation which is in contradiction to the electron phonon-scattering theory which predicts a constant frequency independent scattering rate above 500 cm^{-1} [35] and this absence of saturation seems to suggest that in addition to electron-phonon scattering, there are other scattering channels which may arise from electronic and spin correlations.

5.4 Spectral Weight analysis

To get the qualitative picture of how spectral weight was distributed with temperature for both samples Bi_2Se_3 and Sb_2Te_3, Figure 23 was plotted which has similar behavior for both samples. Spectral weight increases with an increase in frequency. Giving attention to low frequencies, spectral weight is seen to increase on cooling upto about 10,000 cm^{-1} where spectral weight as a function of temperature seems to merge together implying that the spectral weight is only recovered there and this could be a signature of correlation ef-

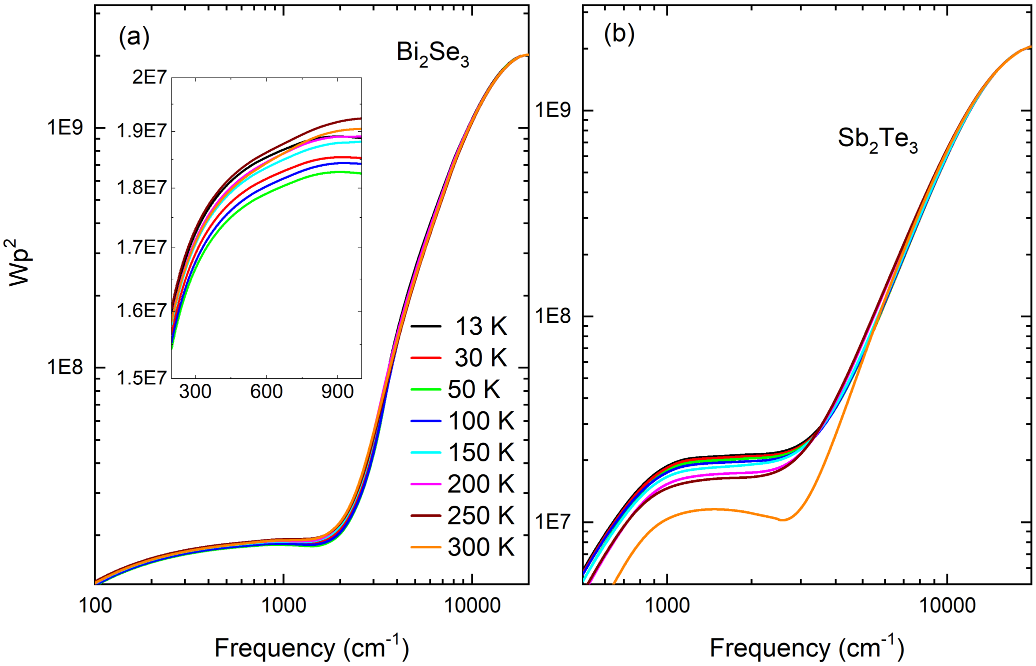

Figure 23: Spectral weight for Bi_2Se_3(a) and Sb_2Te_3(b)samples

fects in the materials. Di Pietro ascribes these low-energy electrodynamics in single crystals of topological insulators, to be influenced by 3D charge excitations [45]. An upturn at about 1000 cm^{-1} to 5000 cm^{-1} in both materials is observed in the spectral weight curves which indicates the spectral weight redistribution beginning in this frequency. The curves do not show any step like features or saturation to show evidence of plasma frequency which could be due to gradual monotonic decrease of reflectivity with increase in frequency as earlier seen.

Chapter 6

6 CONCLUSION AND RECOMMENDATION

In conclusion, this dissertation has delved into the optical properties of two important topological insulators, namely Bi_2Se_3 and Sb_2Te_3, using optical spectroscopy reflection measurements. Through the calculation of optical conductivity via Kramers-Kronig analysis, a comprehensive analysis employing the extended Drude analysis and spectral weight analysis has been conducted on both samples.

The resistivity for both samples shows a metallic behavior, i.e., resistivity decreases with decreasing temperature, with high RRR (1.80 for Bi_2Se_3 and 7.51 for Sb_2Te_3) indicating more pure samples compared to results reported in Ref. [31] and Ref. [36] (7.1354 for Sb_2Te_3 and 1.74 for Bi_2Se_3). We have experimentally found that the bulk optical conductivity of Bi_2Se_3 shows a linear frequency dependence in frequency range from 1500 to 3000 cm^{-1} while Sb_2Te_3 shows no linearity at all frequencies. The linearity of Bi_2Se_3 emerges as a cumulative effect of transitions between the bands with complex dispersion. The spectral weight analysis offers insights into the distribution of optical weight with temperature and frequency, indicating the influence of correlation effects and charge excitations on the material's low-energy electrodynamics.

Based on the results obtained from the measurements of the Bi_2Se_3 sample crystal, several key conclusions can be drawn: The reflectivity measurements reveal significant insights into the metallic behavior of Bi_2Se_3. The presence of a plasma-like feature, attributed to Dirac surface states, indicates strong metallic behavior. The observed direct band gap between 3000 to 4000 cm^{-1} and interband transitions further characterize the material's optical properties, with interband transitions showing temperature dependence in the MIR and no temperarture dependence in the NIR region, highlighting the com-

plex nature of the material's electronic structure. The observed linearity in conductivity in the broad range 1500 cm^{-1} to 3000 cm^{-1} suggests the presence of three dimensional linear electronic bands with band crossings near the chemical potential. Furthermore, the conductivity analysis, including the real and imaginary parts, provides detailed information about charge carrier behavior and scattering mechanisms in Bi_2Se_3. The presence of Drude-like modes and linearity in conductivity suggests the influence of electron-phonon coupling and electronic band structure on charge transport. Additionally, extended Drude analysis reveals the temperature dependence of effective mass with a departure from the simple Drude response observed up to 1000 cm^{-1} indicating the presence of strong electron phonon coupling in the material. An absence of saturation in the scattering rate is observed suggesting that in addition to electron-phonon scattering, there are additional scattering channels which may arise electronic and spin correlations. the spectral weight analysis showed no evidence of plasma frequency, which could have been due to gradual monotonic decrease of reflectivity with increase in frequency.
In terms of reflectivity for Sb_2Te_3, temperature-dependent trends reveal complex spectral weight transfers in the frequency range 1100 to 1300 cm^{-1} and interband transitions showing temperature dependence from 1200 cm^{-1} to 10,000 cm^{-1}, above which it shows no temperature dependence. The appearance of a near-infrared (NIR) band in the optical conductivity spectrum underscores the significance of interband transitions, challenging conventional Drude theory predictions. Conductivity analysis unveils intriguing phenomena in that at low frequencies, conductivity decreases with increasing temperature up to about 2000 cm^{-1} due to phonon scattering, above which it increases with frequency, accompanied by the emergence of a NIR band. No linearity is observed in the conductivity due to the absence of cumulative effect of transitions within the bands with complex dispersion. Furthermore, the extended Drude analysis provides deeper insights into many-body interactions, revealing the influence of electron-phonon coupling and correlation

effects on charge carrier behavior. The observed increase in effective mass with frequency up to 1000 cm^{-1} indicates strong electron-phonon coupling, while the non-saturation of the scattering rate beyond 1200 cm^{-1} implies additional scattering channels beyond electron-phonon interactions.

The Calibration of the Perkin Elmer lambda 1050+ spectrometer at the university of Dar es salaam was not a success, as only part of the data obtained using the Perkin Elmer lambda 1050+ could match with the standard calibration data (6000 to 8500 cm^{-1} for Bi_2Se_3 and 5000 to 12000 cm^{-1} for Sb_2Te_3) obtained using the Bruker Vertex 80 spectrometer, which is a standard and more accurate reflectivity measurement equipment for small samples as the ones used in this research. The failure was due to lack of sample holders for the Perkin Elmer Lambda 1050+ Spectrometer, as well as the inability to perform the Experiment in a dark room thus making the light from the environment to interfere with the accurate data collection. The findings presented in this dissertation significantly contribute to the understanding of Sb_2Te_3's and Bi_2Se_3's electronic and optical properties. The identified trends underscore the materials' potential for various applications, including electronic and optoelectronic devices. Moving forward, further research into the underlying mechanisms driving these behaviors will be crucial for harnessing the full potential of Sb_2Te_3 and Bi_2Se_3 in future technological advancements.

References

[1] G. Azzolina, R. Bertoni, and E. Collet. General landau theory of non-symmetry-breaking and symmetry-breaking spin transition materials. *Journal of Applied Physics*, 129(8), 2021.

[2] P. J. McCann. Geometry and the integer quantum hall effect. *Geometric Analysis and Lie Theory in Mathematics and Physics*, pages 132–208, 1998.

[3] D. N. Sheng, Z. Y. Weng, L. Sheng, and F. D. M. Haldane. Quantum spin-hall effect and topologically invariant chern numbers. *Physical review letters*, 97(3):036808, 2006.

[4] D. Hsieh, D. Qian, L. Wray, Y. Xia, Y. S. Hor, R. J. Cava, and M. Z. Hasan. A topological dirac insulator in a quantum spin hall phase. *Nature*, 452(7190):970–974, 2008.

[5] J. E. Moore. The birth of topological insulators. *Nature*, 464(7286):194–198, 2010.

[6] B. A. Bernevig, T. L. Hughes, and S. Zhang. Quantum spin hall effect and topological phase transition in hgte quantum wells. *science*, 314(5806):1757–1761, 2006.

[7] M. Konig, S. Wiedmann, C. Brune, A. Roth, H. Buhmann, L. W. Molenkamp, X. Qi, and S. Zhang. Quantum spin hall insulator state in hgte quantum wells. *Science*, 318(5851):766–770, 2007.

[8] Y. S. Hor, A. Richardella, P. Roushan, Y. Xia, J. G. Checkelsky, A. Yazdani, M. Z. Hasan, N. P. Ong, and R. J. Cava. p-type bi 2 se 3 for topological insulator and low-temperature thermoelectric applications. *Physical Review B*, 79(19):195208, 2009.

[9] Y. Xia, D. Qian, D. Hsieh, L. Wray, A. Pal, H. Lin, A. Bansil, D. Grauer, Y. S. Hor, R. J. Cava, et al. Observation of a large-gap topological-insulator class with a single dirac cone on the surface. *Nature physics*, 5(6):398–402, 2009.

[10] D. Hsieh, Y. Xia, D. Qian, L. Wray, F. Meier, J. Osterwalder, L. Patthey, J. G. Checkelsky, N. P. Ong, A. V. Fedorov, et al. First observation of spin-momentum helical locking in bi2se3 and bi2te3, demonstration of topological-order at 300k and a realization of topological-transport-regime. *arXiv preprint arXiv:1001.1590*, 2010.

[11] D. Hsieh, Y. Xia, D. Qian, L. Wray, F. Meier, J. H. Dil, J. Osterwalder, L. Patthey, A. V. Fedorov, H. Lin, et al. Observation of time-reversal-protected single-dirac-cone topological-insulator states in bi 2 te 3 and sb 2 te 3. *Physical review letters*, 103(14):146401, 2009.

[12] M. Dressel and G. Grüner. *Electrodynamics of Solids: Optical Properties of Electrons in Matter*. Cambridge University Press, 2002.

[13] G. Chanda. Terahertz and infrared spectroscopy of novel superconductors. 2014.

[14] T. Nicolet and C. All. Introduction to fourier transform infrared spectrometry. *Thermo Nicolet Corporation*, 2001.

[15] M. Z. Hasan and C. L. Kane. Topological insulators. *Reviews of Modern Physics*, 82:3045–3067, 2010.

[16] Y. et al. Xia. Observation of a large-gap topological-insulator class with a single dirac cone on the surface. *Nature Physics*, 5(6):398–402, 2009.

[17] Y. L. et al. Chen. Experimental realization of a three-dimensional topological insulator, bi2te3. *Science*, 325(5937):178–181, 2009.

[18] S. Y. et al. Xu. Observation of fermi arc surface states in a topological metal. *Science*, 347(6219):294–298, 2014.

[19] X. L. Qi and S. C. Zhang. Topological insulators and superconductors. *Reviews of Modern Physics*, 83(4):1057–1110, 2011.

[20] D. et al. Hsieh. Observation of unconventional quantum spin textures in topological insulators. *Science*, 323(5916):919–922, 2009.

[21] D. N. Basov and R. D. Averitt. Imaging the conductance of topological insulators with noninvasive voltage-contrast scanning microwave microscopy. *Physical Review Letters*, 107(17):177602, 2011.

[22] J. W. et al. McIver. Control over topological insulator photocurrents with light polarization. *Nature Nanotechnology*, 7(2):96–100, 2012.

[23] L. et al. Wu. A high-mobility electronic system at an electrolyte-gated oxide surface. *Nature Communications*, 6:6080, 2015.

[24] Frank Padera and CT Shelton. Uv/vis spectroscopy.

[25] C. S. Hsu et al. Infrared spectroscopy. *Handbook of instrumental techniques for analytical chemistry*, 249, 1997.

[26] B. Stuart. Infrared spectroscopy. *Kirk-Othmer encyclopedia of chemical technology*, 2000.

[27] L. M. Ng and R. Simmons. Infrared spectroscopy. *Analytical chemistry*, 71(12):343–350, 1999.

[28] Vertex 80 and 80v ft-ir spectrometers.

[29] A. D. LaForge, A. Frenzel, B. C. Pursley, T. Lin, X. Liu, J. Shi, and D. N. Basov. Optical characterization of bi 2 se 3 in a magnetic field: Infrared evidence for magnetoelectric coupling in a topological insulator material. *Physical Review B*, 81(12):125120, 2010.

[30] F. Gervais. Optical conductivity of oxides. *Materials Science and Engineering: R: Reports*, 39(2-3):29–92, 2002.

[31] R. Sultana, G. Gurjar, S. Patnaik, and V. P. S. Awana. Crystal growth and characterization of bulk sb2te3 topological insulator. *Materials Research Express*, 5(4):046107, 2018.

[32] P. P. Adhikari. *Optical Study of Inter-band Transitions in Topological Insulators Bi2Se3, Bi2Te3, and Sb2Te3.* PhD thesis, University of Akron, 2017.

[33] E. S. Zhukova, H. Zhang, V. P. Martovitskiy, Y. G. Selivanov, B. P. Gorshunov, and M. Dressel. Infrared optical conductivity of bulk bi2te2se. *Crystals*, 10(7):553, 2020.

[34] F. Marsiglio. Eliashberg theory: A short review. *Annals of Physics*, 417:168102, 2020.

[35] T. Klitsner and R. O. Pohl. Phonon scattering at silicon crystal surfaces. *Physical Review B*, 36(12):6551, 1987.

[36] O. Chiatti, C. Riha, D. Lawrenz, M. Busch, S. Dusari, J. Sánchez-Barriga, A. Mogilatenko, L. V. Yashina, S. Valencia, A. A. Ünal, et al. 2d layered transport properties from topological insulator bi2se3 single crystals and micro flakes. *Scientific Reports*, 6(1):27483, 2016.

[37] N. P. Butch, K. Kirshenbaum, P. Syers, A. B. Sushkov, G. S. Jenkins, H. D. Drew, and J. Paglione. Strong surface scattering in ultrahigh-mobility bi 2 se 3 topological insulator crystals. *Physical Review B*, 81(24):241301, 2010.

[38] A. D. LaForge, A. Frenzel, B. C. Pursley, T. Lin, X. Liu, J. Shi, and D. N. Basov. Optical characterization of bi 2 se 3 in a magnetic field: Infrared evidence for magnetoelectric coupling in a topological insulator material. *Physical Review B*, 81(12):125120, 2010.

[39] P. Di Pietro, F. M. Vitucci, D. Nicoletti, L. Baldassarre, P. Calvani, R. Cava, Y. S. Hor, U. Schade, and S. Lupi. Optical conductivity of bismuth-based topological insulators. *Physical Review B*, 86(4):045439, 2012.

[40] D. L. Greenaway and G. Harbeke. Band structure of bismuth telluride, bismuth selenide and their respective alloys. *Journal of Physics and Chemistry of Solids*, 26(10):1585–1604, 1965.

[41] A. V. Pronin and M. Dressel. Nodal semimetals: A survey on optical conductivity. *physica status solidi (b)*, 258(1):2000027, 2021.

[42] F. Hütt, A. Yaresko, M. B. Schilling, C. Shekhar, C. Felser, M. Dressel, and A. V. Pronin. Linear-in-frequency optical conductivity in gdptbi due to transitions near the triple points. *Physical Review Letters*, 121(17):176601, 2018.

[43] R. E. Glover III and M. S Tinkham. Conductivity of superconducting films for photon energies between 0.3 and 4 0 k t c. *Physical Review*, 108(2):243, 1957.

[44] S. Kaiser, C. R. Hunt, D. Nicoletti, W. Hu, I. Gierz, H. Y. Liu, M. Le Tacon, T. Loew, D. Haug, B. Keimer, et al. Optically induced coherent transport far above t c in underdoped yba 2 cu 3 o 6+ δ. *Physical Review B*, 89(18):184516, 2014.

[45] P. Di Pietro, F. M. Vitucci, D. Nicoletti, L. Baldassarre, P. Calvani, R. Cava, Y. S. Hor, U. Schade, and S. Lupi. Optical conductivity of bismuth-based topological insulators. *Physical Review B*, 86(4):045439, 2012.